frontiers | Frontiers in Earth Science

TYPE Original Research
PUBLISHED 09 February 2023
DOI 10.3389/feart.2023.1085313

OPEN ACCESS

EDITED BY
Fanwei Meng,
China University of Mining and Technology, China

REVIEWED BY
Tao Yang,
Nanjing University, China
Dongya Zhu,
SINOPEC Petroleum Exploration and Production Research Institute, China

*CORRESPONDENCE
Zhong Li,
lizhong@mail.igcas.ac.cn

SPECIALTY SECTION
This article was submitted to Sedimentology, Stratigraphy and Diagenesis, a section of the journal Frontiers in Earth Science

RECEIVED 31 October 2022
ACCEPTED 26 January 2023
PUBLISHED 09 February 2023

CITATION
Zhou Y and Li Z (2023), Terminal Ediacaran microbialite lithofacies associations with paleo-environmental constraints in a high-frequency sequence stratigraphic framework of Sichuan Basin, SW China. *Front. Earth Sci.* 11:1085313. doi: 10.3389/feart.2023.1085313

Terminal Ediacaran microbialite lithofacies associations with paleo-environmental constraints in a high-frequency sequence stratigraphic framework of Sichuan Basin, SW China

Yuanquan Zhou[1,2,3] and Zhong Li[1,2,3]*

[1]State Key Laboratory of Lithospheric Evolution, Institute of Geology and Geophysics, Chinese Academy of Sciences, Beijing, China, [2]Innovation Academy for Earth Science, Chinese Academy of Sciences, Beijing, China, [3]University of Chinese Academy of Sciences, Beijing, China

The terminal Ediacaran shallow marine microbialites are significant for paleo-environment reconstruction and petroleum exploration. Their depositional and paleo-environmental characteristics during high-frequency sea-level fluctuations were paid less attention, which limited the understanding of their evolution and related reservoir characterization. Microbialites from the fourth member of the upper Ediacaran Dengying Formation, Gaoshiti-Moxi area, Sichuan Basin, SW China are important records for studying their lithofacies associations and paleo-environmental constraints in high-frequency depositional sequences. Petrographic and geochemical analyses (*in-situ* major and trace elements and carbon and oxygen isotopes) indicate microbialites depositional and paleo-environmental evolution on a rimmed platform within a fourth-order depositional sequence. From late TST (transgressive systems tract) to early HST (highstand systems tract), thick-bedded dark-grey dolomudstone-thin-bedded spotted thrombolite dominates the platform margin; while thick-bedded dark-grey dolomudstone-thin bedded dark-grey wavy stromatolite dominates the platform interior. From late HST to early TST of the next fourth-order sequence, the platform margin is dominated by thick-bedded spotted thrombolite—dolograinstone, while the carbonate interior is dominated by thin-medium-bedded layered thrombolite—light-grey wavy stromatolite. Salinity correlates well with microbialite lithofacies associations: the platform interior layered thrombolite and wavy stromatolite enriched lithofacies associations are characterized by higher salinity than that of the platform margin spotted thrombolite enriched lithofacies associations. The microbialite lithofacies associations are less constrained by redox: platform interior layered thrombolite and wavy stromatolite enriched lithofacies associations are slightly more reduced than the platform interior spotted thrombolite enriched lithofacies associations. The redox analysis of the microbialites also indicates low oxygen levels of shallow marine in the study area during terminal Ediacaran, with possible oxygenation at the Ediacaran-Cambrian boundary. The study suggests that the terminal Ediacaran microbialite development was controlled by both high-frequency sea-level fluctuations and paleo-environmental factors such as salinity and redox. Platform margin spotted thrombolitic reefs from late fourth-order HST to next early fourth-order TST serve as favorable microbialite reservoirs. Platform interior layered thrombolites

and wavy stromatolites are regarded as potential reservoirs, which deserve more detailed depositional-paleo-environmental research.

KEYWORDS

terminal Ediacaran, microbialite, high-frequency sequence, salinity, redox

1 Introduction

The Ediacaran—Cambrian transition is crucial in Earth history, during which a set of bioevolutionary innovations occurred, such as metazoan explosion, oxygen levels significant increase and great seawater salinity reduction (Knauth, 2005; Lyons et al., 2014; de Oliveira et al., 2019). Microbialites, a component of marine ecological system and seawater chemistry evolution, have been broadly used to restore the paleo-oceanographic and paleo-environmental information about the setting in which they develop (Burne and Moore, 1987; Grotzinger and Knoll, 1999; Riding, 2000; Li A. et al., 2021). As the terminal Ediacaran microbialite is considered as a major sedimentary carrier of prokaryotic communities and activities (Li F. et al., 2021), its sedimentological study may shed light on the evolution of related carbonate buildups and paleo-environment during the Ediacaran—Cambrian transition. Additionally, these microbialites host economic petroleum reserves worldwide, such as the Ara Group in the Sultanate of Oman (Schröder et al., 2005) and the Dengying Formation in South China (Hu et al., 2020). The sedimentological and paleo-environmenal investigation would also provide valuable information for characterizing the distribution and scale of these microbialite reservoirs, which may also facilitate future petroleum exploration.

Previous studies on terminal Ediacaran microbialites have been largely focused on their petrology and general depositional architecture (Grotzinger and James, 2000; Jiang et al., 2003; Grotzinger and Al-Rawahi, 2014; Ding et al., 2021), while the spatial distribution of these microbialite lithofacies is still controversial. For example, studies by Guo et al. (2020), Li A. et al. (2021) and Peng et al. (2021) indicate that terminal Ediacaran thrombolites were well-developed in sub-tidal environments and stromatolites were flourished in inter-tidal settings. However, other studies hold the opposite view (Harwood and Summer 2011; Luo et al., 2022; Wang et al., 2022). Compared with studies on distribution patterns of terminal Ediacaran microbialite lithofacies or lithofacies associations in a third-order depositional sequence (Schröder et al., 2005; Ding et al., 2019; Lan et al., 2022a), investigations on their distribution patterns within high-frequency sequences are relatively scarce. Precise distribution of these microbialite lithofacies or lithofacies associations in high-frequency depositional sequences should be studied further.

As the environmental constraints of Phanerozoic shallow marine carbonate factories (nutrients, salinity, temperature, seawater energy and transparency, *etc.*) are based on the study on the well-understood habitats of metazoans (Pomar, 2001; Pittet et al., 2002; Pomar and Haq, 2016), they cannot be all directly used to analyze the paleo-environment of Precambrian microbialite-dominated carbonate factories (Preto et al., 2019). Recent studies proposed that salinity and redox are important environmental constraints for microbialites: thrombolites prefer low-salinity and less oxygenated environments, while stromatolites are more developed in high-salinity and more oxygenated environments (Suarez-Gonzalez et al., 2019; Chen et al., 2021; Lan et al., 2022b; Tang et al., 2022). Nevertheless, in most cases, the judgement of salinity and redox is mainly based on qualitative petrographic characteristics, rather than quantitative geochemical evidences. More systematic studies, integrating petrography, stratigraphy and geochemistry on the terminal Ediacaran microbialites are needed, which may enhance the understanding of their evolution and ambient seawater chemistry.

In recent studies on life and environment co-evolution during Ediacaran—Cambrian transition, the microbialites of the upper Ediacaran Dengying Formation in South China have been frequently chosen as research objects (Guo et al., 2013; Shields-Zhou et al., 2013; Gao et al., 2016). Petrographic and environmental studies have been mainly conducted on microbialite samples from outcrops in the peripheral Sichuan Basin (Ding et al., 2022; Lan et al., 2022b; Li et al., 2022), while less attention has been paid to the microbialites in the basin interior due to outcrop scarcity. Moreover, in the central Sichuan Basin, the upper Ediacaran Dengying Formation hosts a giant gas field, with proven natural gas reserves of 5908×10^8 m^3 for the fourth member by the end of 2020 (Yan et al., 2022). In this study, careful petrographic observation and geochemical tests (*in-situ* major and trace elements (including REE) and carbon and oxygen isotopes) are conducted on samples collected from a series of wells in the central Sichuan Basin. The study aims to (i) identify the microbialite lithofacies associations in a fourth-order sequence stratigraphic framework; (ii) analyze the salinity and redox conditions of the lithofacies associations using proper geochemical proxies; (iii) build up a depositional - paleo-environmental evolution model for these microbialites in a fourth-order depositional sequence and evaluate their reservoir potential.

2 Geological setting

The Sichuan Basin is a 18.8 km^2 diamond-shaped sedimentary basin in southwest China (Zhao and Cawood, 2012), which is tectonically located in the western Yangtze craton and bounded by the Longmenshan Fold Belt, Micangshan Uplift, Dabashan Fold Belt, Hubei-Hunan-Guizhou Fold Belt and Emeishan—Liangshan Fold Belt (Ma et al., 2007) (Figure 1A). The basin is constituted by several structural units: Central Uplift, Northwest Depression and Southeast Depression. The Central Uplift is a inherited nose-shaped paleo-uplift initiated from Ediacaran and is the location of the study area, Gaoshiti - Moxi area (Figure 1B). Influenced by the Rodinia break-up, the Ediacaran Sichuan basin was in an extensional state (Zhu et al., 2007). Triggered by the related basement faults, Deyang—Anyue Rift, a NS-trending rift, developed to the east of the Gaoshiti—Moxi uplift (Li et al., 2015; Wei et al., 2015; Liu et al., 2016).

As a result of large-scale transgression after the Marinoan glaciation, the Ediacaran strata are widely-distributed on the Yangtze craton (Jiang et al., 2011). They are composed by the

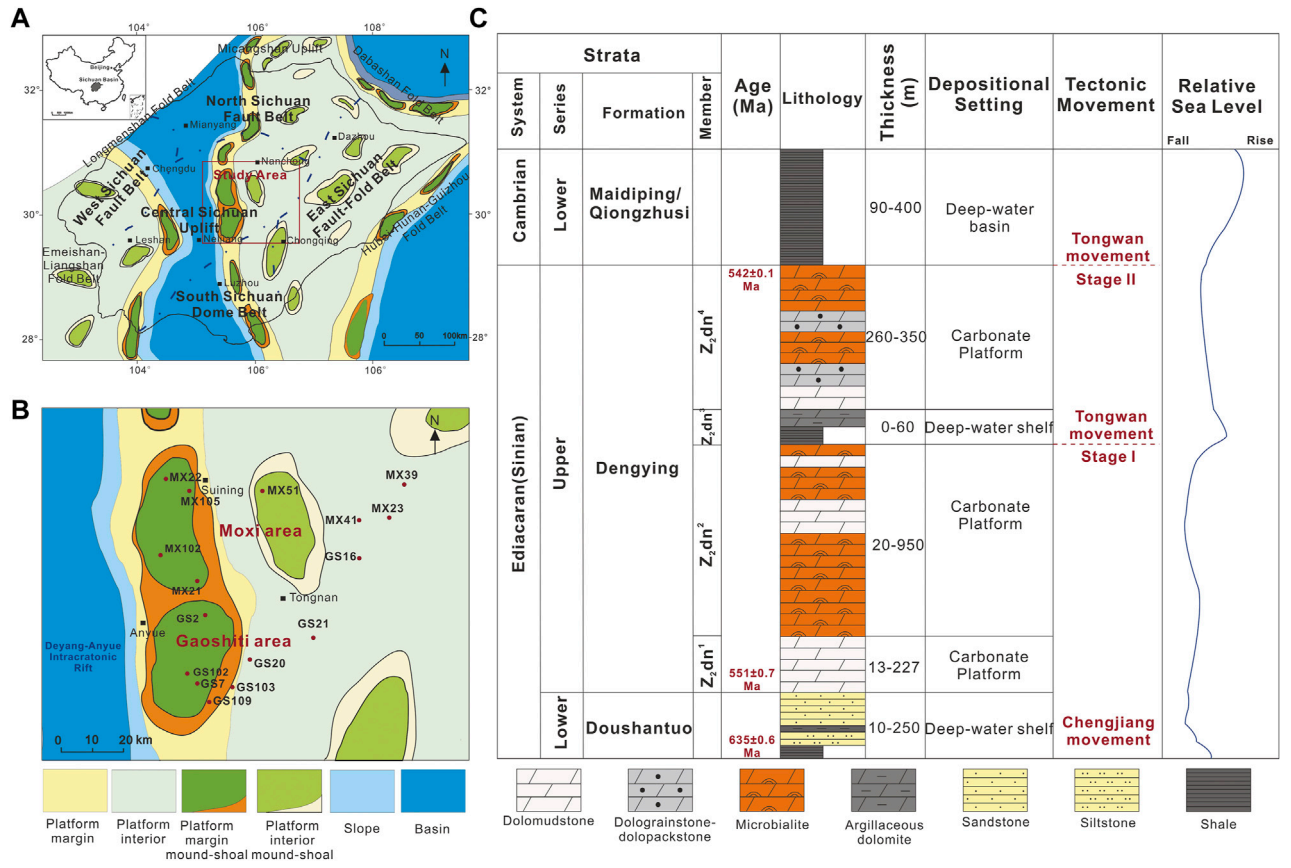

FIGURE 1
Geological setting of the Gaoshiti—Moxi area. **(A)** Location of the Gaoshiti—Moxi area in the Sichuan Basin (modified from Wang et al., 2021; Lan et al., 2022b). **(B)** Wells distribution in the Gaoshiti—Moxi area. **(C)** Stratigraphic column of the Dengying Formation in the Gaoshiti—Moxi area (modified from Hu et al., 2018; Zhou et al., 2020; Wang et al., 2021; the age data are from Condon et al., 2005; Chen et al., 2015).

Doushantuo Formation and the Dengying Formation, with a total thickness of more than 2000 m (Zhu et al., 2015). By zircon U-Pb dating of the volcanic ash, the bottom and top of the Dengying Formation are restricted to 551 ± 0.7 Ma and 542 ± 0.1 Ma (Condon et al., 2005; Chen et al., 2015). The Dengying Formation is 600–1000 m thick in the Sichuan Basin (Zhang J. et al., 2014), which is divided into four members from bottom to top: Z_2dn^1, Z_2dn^2, Z_2dn^3, and Z_2dn^4. Z_2dn^1 is composed of dolomudstone; Z_2dn^2 is mainly composed of microbialite; Z_2dn^3 consists of siltstone, shale and dolomudstone. Z_2dn^4 is 260–350 m thick and is composed of microbialite, intraclast dolomite and dolomudstone. Influenced by the Tongwan Movement, various extents of erosion occur at top of Z_2dn^2 and Z_2dn^4 (Wen et al., 2020) (Figure 1C).

Previous studies concluded the general depositional architecture of the Gaoshiti -Moxi area as a rimmed carbonate platform (Liu et al., 2015; Li et al., 2020; Wang et al., 2020; Zhou et al., 2020). From west to east, the Z_2dn^4 develops deep-water facies, platform margin mound—shoal facies, platform interior shoal and tidal flat, with distinct lithological differences (Zou et al., 2014). The Gaoshiti—Moxi area is also an important natural gas producing area. According to reservoir property differences, Z_2dn^4 is divided into a lower sub-member and an upper sub-member (Wang et al., 2021). All the samples of the study were collected from the upper sub-member of Z_2dn^4 in a series of wells.

3 Materials and methods

3.1 Sampling strategy

In order to ensure that the studied samples preserve their original depositional records, they were collected from the cores with well-preserved micrite of microbialite fabrics (e.g., laminae and clots) or typical non-microbialites. To avoid the non-carbonate content and the diagenetic products, the sampling positions are far away from vugs, pores, burrow filling or fractures. When acquiring the powder samples for carbon and oxygen isotope analysis, the fresh surface of sample chips were micro-drilled.

3.2 Petrographic observation

200 core samples were selected for thin sections, which were stained using Alizarin Red S to differentiate calcite from dolomite (Dickson, 1966). The thin section study was conducted in the Laboratory of Diagenesis in the Institute of Geology and Geophysics, Chinese Academy of Sciences, Beijing (IGGCAS). The micro-scaled depositional fabrics were carefully differentiated under plane polarized light and cathode luminescence (using a RELIOTRON, model RELION III; 5–8 kV and 300–400 μA gun current).

3.3 Geochemical analyses

3.3.1 *In-situ* major and trace element analysis

Compared with whole rock analysis, *in-situ* analysis of major and trace elements can precisely locate a target area with the least possible visible diagenetic alteration (Kamber and Webb, 2007; Hood and Wallace, 2015), which has been advocated and applied in sedimentological and environmental analysis of microbialites recently (Della Porta et al., 2015). As the microbialites of the Z_2dn^4 in the Gaoshiti—Moxi area have gone though long-term deep burial with multi-stage diagenetic alterations (Hu et al., 2020), even the use of a dental drill cannot completely eliminate the diagenetic contamination. In order to acquire as much as possible the primary depositional records of the microbialites, 23 thickened thin sections were chosen to examine the major and trace element (including rare earth elements with yttrium, REE + Y) compositions by LA-ICP-MS (Laser Ablation Inductively Coupled Plasma Mass Spectrometer) at Wuhan SampleSolution Analytical Technology Co., Ltd., Wuhan, China. Laser sampling was performed by a GeolasPro laser ablation system consisting of a COMPexPro 102 ArFexcimer laser (wavelength 193 nm; maximum energy 200 mJ) and a MicroLas optical system. Ion-signal intensities were acquired by an Agilent 7700e ICP-MS instrument, using a helium carrier gas. The spot size and frequency of the laser were set to 90μm and 5 Hz. Trace element compositions of the samples were calibrated against various reference materials (BHVO-2G, BCR-2G and BIR-1G) without using an internal standard (Liu et al., 2008a). Each analysis included a background acquisition of approximately 20–30 s followed by 50 s of data acquisition from the sample. An Excel-based software ICPMSDataCal was applied to perform off-line selection and integration of background and analyzed signals, time-drift correction and quantitative calibration (Liu et al., 2008b). Trace element values were normalized to the upper continental crust (UCC) (Taylor and McClennan, 1985) and the REE + Y values were normalized to standard Post-Archean Average Shale (PAAS) (McLennan, 1989).

3.3.2 Carbon and oxygen isotopes

23 powder samples were micro-drilled on the matrix dolostones to conduct carbon and oxygen isotope analysis at the Laboratory for Stable Isotope Geochemistry, IGGCAS. Samples (each 0.3–0.8 mg) were reacted for 10 h using the common acid bath method at 90°C and the CO_2 produced was analyzed with a Finnigan-MAT 252 mass spectrometer (Land et al., 1980; Vahrenkamp and Swart, 1994). The results were presented in parts per thousand (delta units) with respect to the Vienna Pee Dee Belemnite (V-PDB) standard. The typical standard deviation of a set of 10 individual measurements yielded one σ values <0.15‰ for $\delta^{13}C$ and <0.20‰ for $\delta^{18}O$. The precision for both $\delta^{13}C$ and $\delta^{18}O$ measurements was better than ±0.1‰.

4 Results

4.1 Petrography

The lithology of the Z_2dn^4 in the study area is divided into microbialite and non-microbialite. The microbialites are further classified into wavy stromatolite, spotted thrombolite and layered thrombolite mainly according to meso-scale microbial fabrics (Riding, 2000). Based on Dunham classification (1962), the non-microbialites are further mainly divided into dolograinstone, dolopackstone, light-grey dolomudstone and dark-grey dolomudstone.

4.1.1 Microbialite

Wavy stromatolite. Wavy stromatolites, characterized by distinct dense and wavy laminae, are well-developed in the study area. According to the color difference, they are further classified into "light-grey wavy stromatolites" (Figure 2A) and "dark-grey wavy stromatolites" (Figure 2B). Under the plane polarized light, the typical wavy matrix of both dark-grey wavy stromatolites and light-grey wavy stromatolites can be observed, with "Girvallena-like" fabric (Figure 3A, C. In light-grey wavy stromatolites, light-grey micro-crystalline to coarse-crystalline cements develop between the matrix layers, which are red to bright red under cathode luminescence (CL) (Figure 3B). In contrast, dark-grey micro-crystalline cements are distributed between the matrix layers of dark-grey wavy stromatolites, which is dull red or non-luminescent under CL. Wavy stromatolites are more developed in platform interior in general.

Spotted thrombolite. Thrombolites are characterized by macroscopically clotted fabrics (Riding, 2000). In the study area, the thrombolites with chaotic-distributed clotted fabrics on the cores are classified as "spotted thrombolite", which are predominantly grey to dark-grey (Figures 2C,D). Under plane polarized light, the matrix, the dark-grey clotted micritic dolomite (mesoclot) is characterized by Renalcis-like fabrics (Figures 3D,E). Under CL, the micro-crystalline, medium-crystalline and coarse-crystalline cements are dull red, red and bright red, respectively (Figure 3F). Contrary to wavy stromatolites, spotted thrombolites are mainly distributed in platform margin.

Layered thrombolite. The thrombolites with horizontally-distributed clotted fabrics are classified as "layered thrombolites", which are often dark-grey on the cores (Figure 2E). The matrix is also characterized by "Renalcis-like" fabrics under plane polarized light (Figure 3G). Although layered thrombolites can be observed in both platform margin and platform interior, they are more developed in platform interior.

4.1.2 Non-microbialite

Dolograinstone. Dolograinstones are light-gray to brownish gray and are thick-bedded or massive structured on the cores (Figure 2F). Under plane polarized light, the grains are composed of well-sorted rounded sand-sized intraclasts, ooids, oncoids, and peloids, with diameters ranging from 0.1 to 0.3 mm (Figure 3H). Fragments of stromatolites and thrombolites can be observed occasionally. Dolograinstones are observed in platform margin.

Dolopackstone. Dolopackstones are gray to brownish gray and are medium-bedded to thin-bedded structured on the cores (Figure 2G). Under plane polarized light, the grains are composed of sub-rounded to rounded intraclasts and peloids, with diameters ranging from 0.05 to 0.1 mm (Figure 3I). Stromatolite fragments are often observed. Dolopackstones are more developed in platform interior.

Dark-grey dolomudstone. Dark-grey dolomudstones are dark-grey or even black, which are more frequently distributed in platform interior (Figure 2H).

Light-grey dolomudstone. Compared with dark-grey dolomudstones, light-grey dolomudstones are much lighter in color. A few stromatolite laminae and thrombolite clots can be observed on thin sections (Figure 2I). Light-gray dolomudstones

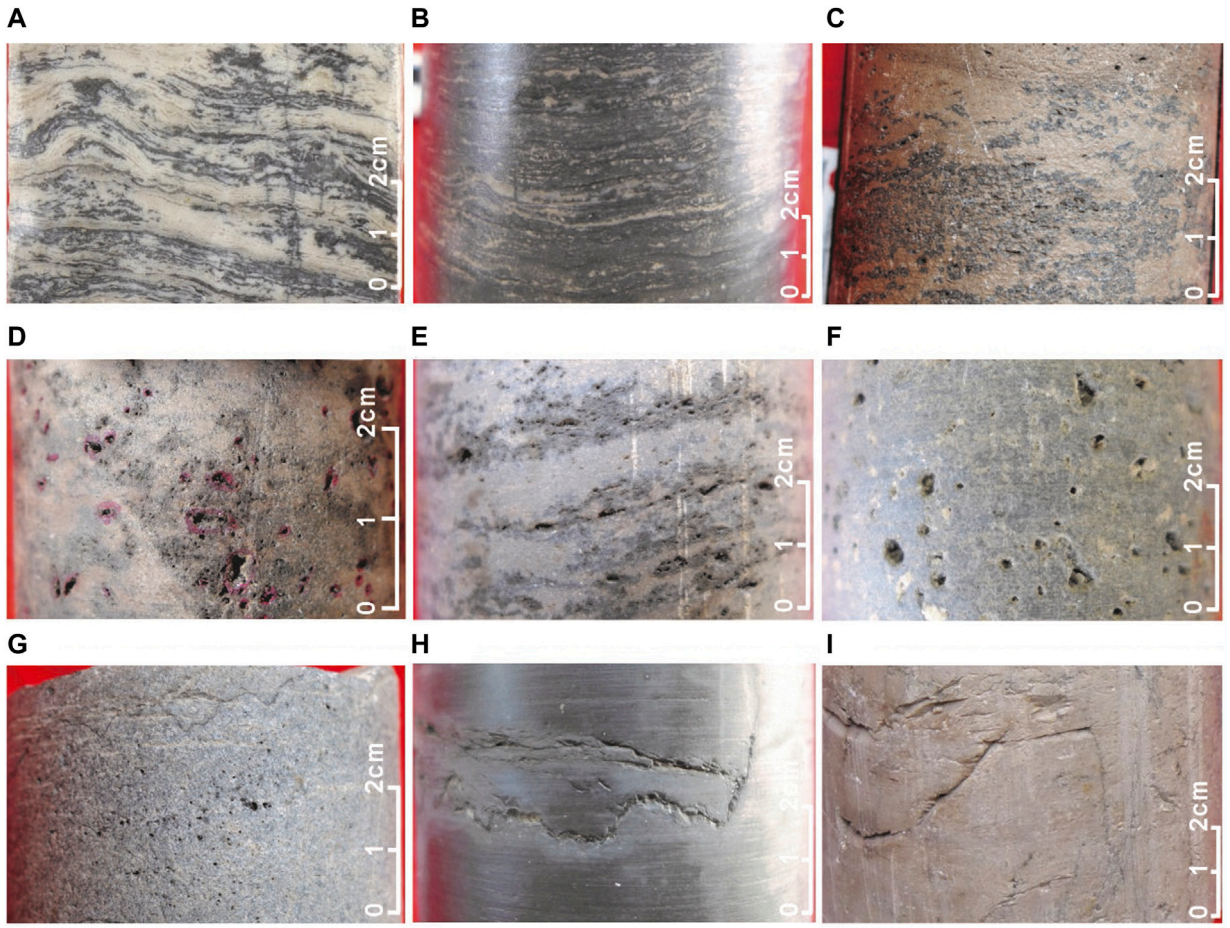

FIGURE 2
Cores of main microbialites and non-microbialites types. **(A)** MX105, 5335.14 m, light-grey wavy stromatolite. **(B)** MX105, 5356.27 m, dark-grey wavy stromatolite. **(C)** GS7, 5325.52 m, spotted thrombolite. **(D)** MX105, 5316.88 m, spotted thrombolite. **(E)** MX105, 5323.45 m, layered thrombolite. **(F)** MX105, 5303.14 m, dolograinstone. **(G)** GS16, 5452.86 m, dolopackstone. **(H)** MX105, 5362.15 m, dark-grey dolomudstone. **(I)** GS21, 5284 m, light-grey dolomudstone.

are more developed in platform interior, with occurrence of bird-eye structures.

Dolomitized karst breccia. This lithofacies is well-developed in the upper Z_2dn^4 close to or at the Ediacaran—Cambrian boundary. They are mainly brown and less than 1 m thick. Most karst breccias are angular to sub-angular and infilled with dolomitic mud.

4.2 High-frequency sequence stratigraphy

Based on outcrop observation and 3D seismic interpretation with well log calibration, the Dengying Formation in the Gaoshiti - Moxi area can be divided into two third-order depositional sequences: the first third-order sequence includes Z_2dn^1 (transgressive systems tract, TST) and Z_2dn^2 (highstand systems tract, HST); the second third-order sequence is composed of Z_2dn^3 (TST) and Z_2dn^4(HST) (Liu et al., 2015; Hu et al., 2018). The third-order sequence boundaries are characterized by regional unconformities of top of Z_2dn^2 and Z_2dn^4 on the outcrops. On the 3D seismic profile, these two third-order sequences are bounded by denudation surfaces or onlap surfaces (Wang et al., 2021).

Following the definition of Haq et al. (1987) and Peropadre et al. (2013), high-frequency sequences are referred to the depositional responses to fourth or higher orders of base-level cycles; and fourth and fifth-order sequences can be divided and correlated by applying the principles of cyclostratigraphy and event stratigraphy. In the study area, fourth-order sequence boundaries can be identified by lithofacies characteristics and mode transitions of well log curves. On the cores, lithofacies sudden changes and exposure-related lithofacies occur at fourth-order sequence boundaries, including karst breccias and dissolution vugs and pores (Zhang et al., 2009; Xu et al., 2020). Characterized by equal spacing sampling, continuous data series and high vertical resolution, well logging data such as GR (gamma ray) curves, KTH (potassium and thorium) curves and FMI (Fullbore Microscan Imager) images are applied as effective tools to classify fourth-order depositional sequences (Peng et al., 2021). The GR values are generally low (below 30 API) and display a box-shaped mode with unobvious jags; however, at lithofacies transitional surfaces, their values increase sharply and transfer to a shallowing-upward trend of finger- or finger-joint-box-shaped curves (Wang et al., 2021). Similarly, the KTH values increase instantly with spikes at fourth-order sequence boundaries. On FMI images, dissolution-related

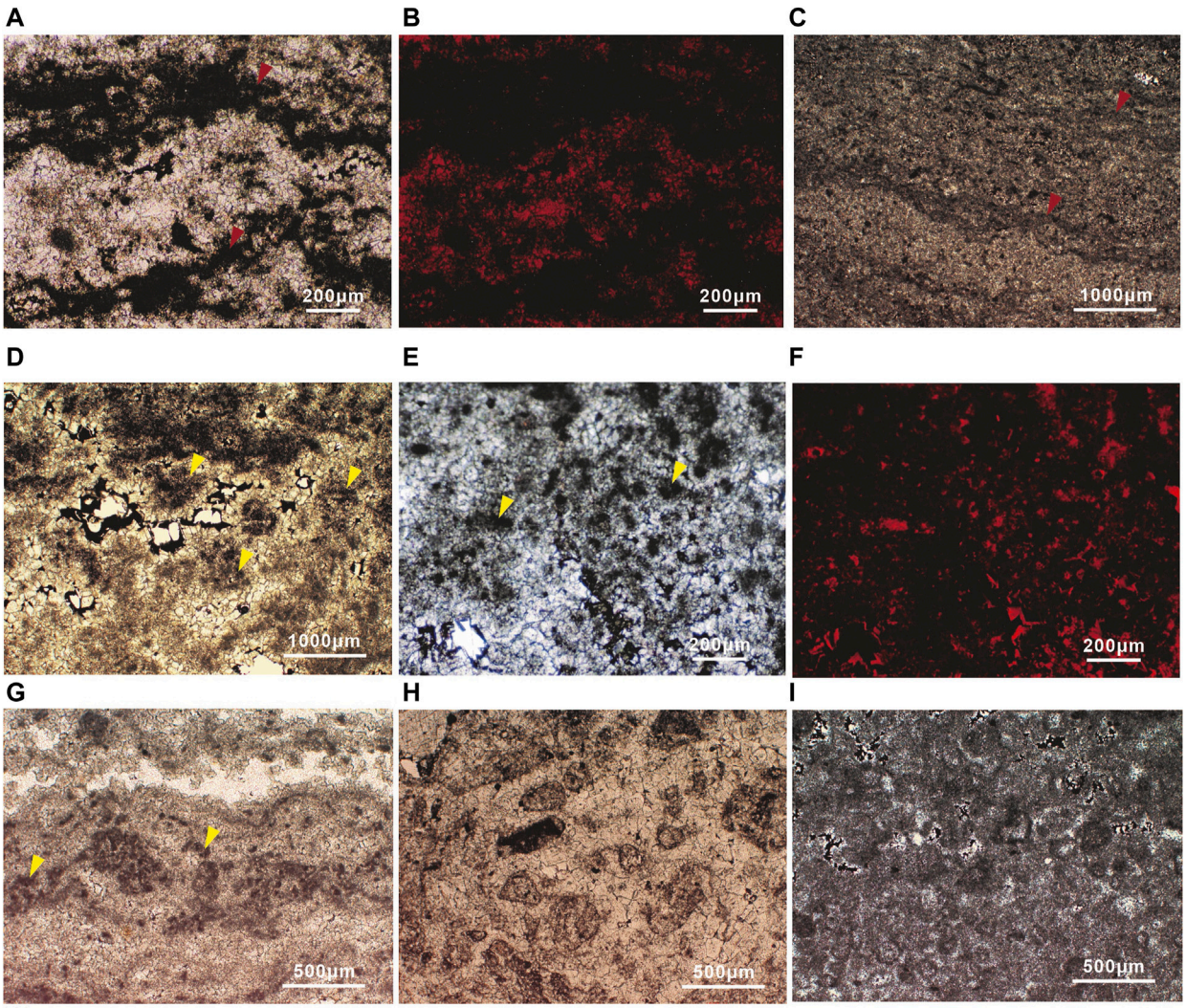

FIGURE 3
Micro-characteristics of main microbialites and non-microbialites. **(A)** MX105, 5359.5 m, light-grey wavy stromatolite. **(B)** **(A)** under cathode luminescence (CL). **(C)** GS21, 5226.36 m, dark-grey wavy stromatolite. **(D)** MX51, 5338.5 m, spotted thrombolite. **(E)** MX39, 5302.6 m, spotted thrombolite. **(F)** **(E)** under CL. **(G)** GS20, 5201.99 m, layered thrombolite. **(H)** MX105, 5303.3 m, dolograinstone. **(I)** GS20, 5220.28 m, dolopackstone. (Red arrows indicate the Girvanella-like fabrics. Yellow arrows indicate the Renalcis-like fabrics).

characteristics such as random dark spots with oblique modes and the sudden mode change that indicates lithofacies transformation can be observed at these high-frequency sequence boundaries (Hu et al., 2018; Wang et al., 2021).

By correlating the GR, KTH and FMI logging data with core observation and a study of recent publications, the Z_2dn^4 of the Gaoshiti - Moxi area is divided into five fourth-order depositional sequences (Figure 4). At the fourth-order sequence boundaries, dolomitized karst breccias are observed on cores and the FMI image suddenly turns chaotic (Wang et al., 2021). Above the sequence boundaries, dark-grey dolomudstones appear and the GR and KTH values increase sharply. The cores shown here are predominantly presented in the last fourth-order depositional sequence (Figure 5). In different stages of a fourth-order depositional sequence, various types of typical lithofacies associations develop in platform margin and platform interior, which are summarized below (Figure 6).

4.2.1 Late TST—early HST

In platform margin, thick-bedded dark-grey dolomudstone overlain by thin-bedded spotted thrombolite is frequently developed, with thickness of each association less than 3 m (Lithofacies Association A). In platform interior, thick-bedded dark-grey dolomudstone overlain by thin-bedded dark-grey wavy stromatolite (Lithofacies Association B) can be observed, with thickness less than 2 m. The other lithofacies association of platform interior, thick-bedded dark-grey dolomudstone overlain by thin-bedded layered thrombolite (Lithofacies Association C) is far less developed.

4.2.2 Late HST—next early TST

From late HST to early TST of the next fourth-order sequence, microbialite lithofacies associations are more diverse. The platform margin develops three types of lithofacies associations: thin-bedded dark-grey dolomudstone—thick-bedded spotted thrombolite

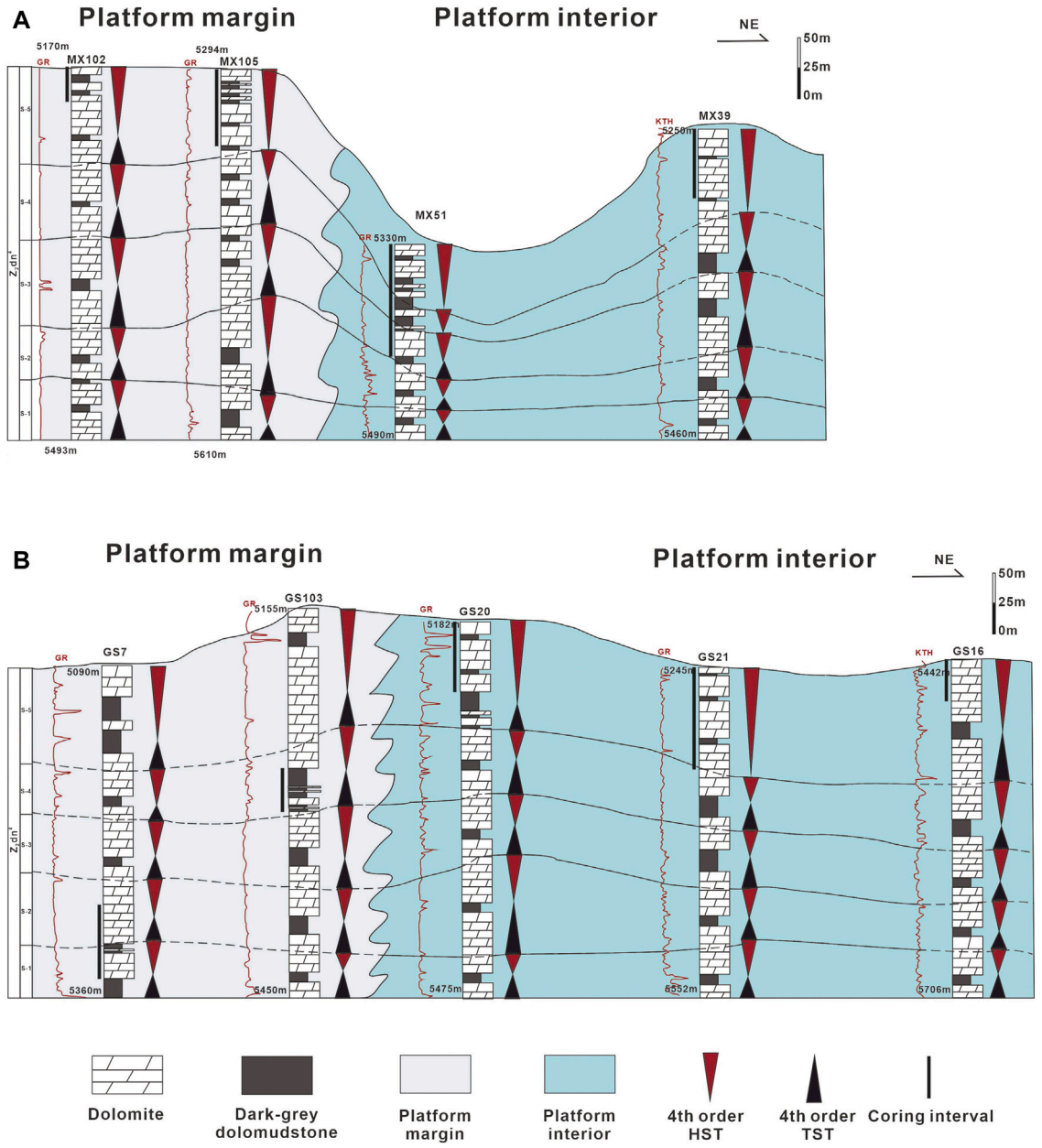

FIGURE 4
Fourth-order sequence stratigraphic classification of the Z_2dn^4 of the Gaoshiti—Moxi area. **(A)** Fourth-order sequence stratigraphic classfication of the Moxi area. **(B)** Fourth-order sequence stratigraphic classification of the Gaoshiti area.

(Lithofacies Association D); thick-bedded spotted thrombolite—dolograinstone (Lithofacies Association E); thin-medium-bedded light-grey wavy stromatolite—light-grey dolomudstone (Lithofacies Association F). The thickness of Lithofacies Associations D and E can reach 15 m, while that of Lithofacies Association F is less than 10 m. The platform interior also develops three types of lithofacies associations: thin-medium-bedded dark-grey dolomudstone—layered thrombolite—wavy stromatolite (Lithofacies Association G); thin-medium-bedded dolopackstone—light-grey wavy stromatolite—light-grey dolomudstone (Lithofacies Association H); thin-bedded layered thrombolite—wavy stromatolite—light-grey dolomudstone (Lithofacies Association I). The thickness of Lithofacies Associations G, H and I is usually less than 8 m. Lithofacies Associations E and H are referred to as "platform margin mound-shoal complex" and "platform interior mound-shoal complex" respectively (Hu et al., 2018; Peng et al., 2021).

4.3 Geochemistry

4.3.1 Major and trace element concentrations and ratios

The Al and trace element concentrations and ratios of the studied samples are summarized in Table 1 (n=23). Most samples are characterized by low Al, Th, Zr and Sc concentrations, with a few

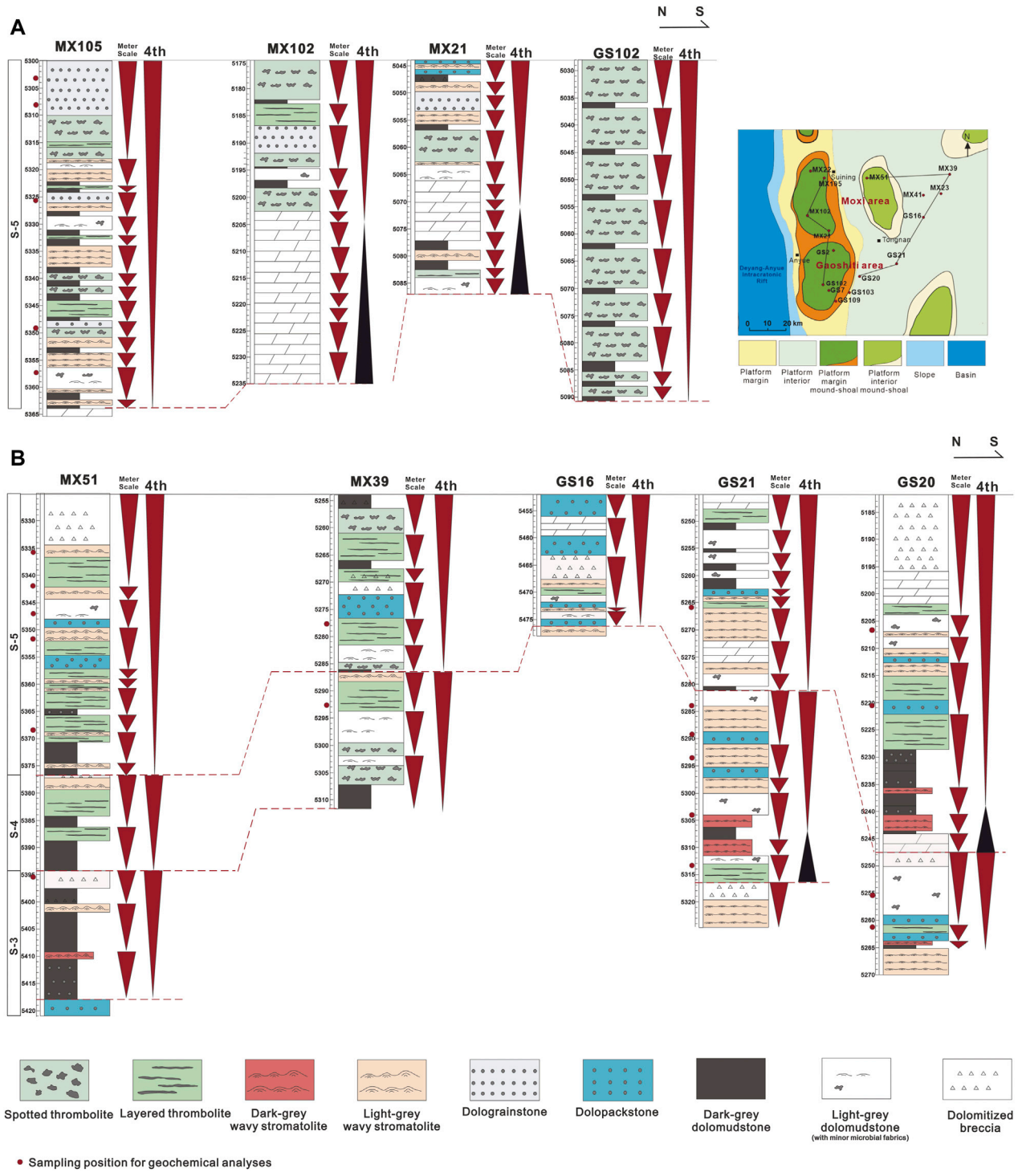

FIGURE 5
Detailed cores distribution in fourth-order sequence stratigraphic frameworks in the Gaoshiti - Moxi area. **(A)** Cores distribution in fourth-order sequence stratigrahpic frameworks in the platform margin. **(B)** Cores distribution in fourth-order sequence stratigrahpic frameworks in the platform interior.

abnormally high values. These matrix dolostones have Al contents ranging from 0.001% to 0.328%, with a mean value of 0.048%. The Th concentrations are between 0.006 ppm and 0.073 ppm (mean value = 0.026 ppm); Zr concentrations are between 0.014 ppm and 3.094 ppm (mean value = 0.453 ppm); and Sc concentrations are between 0.000 ppm and 0.337 ppm (mean value = 0.057 ppm). The Sr/Ba ratios of the studied samples range from 0.680 to 9.258 (mean value = 3.800). The Ba/Nd ratios range from 0.103 to 290.516 (mean value =76.069). And the Mn/Sr ratios are between 1.305 and 23.090 (mean value = 6.437). The REE + Y concentrations, ratios and anomalies of the studied samples are presented in Table 2 (n=23). The total REE (∑REE) concentrations of matrix dolostones are

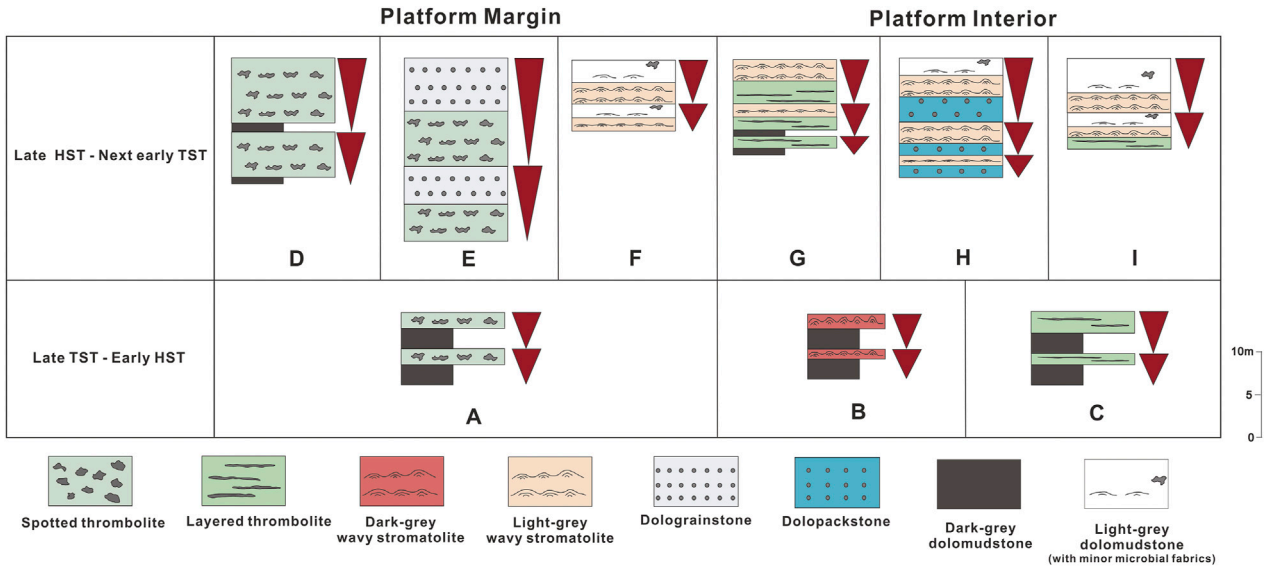

FIGURE 6
Microbialite lithofacies associations of the Z_2dn^4 of the Gaoshiti-Moxi area in a fourth-order sequence stratigraphic framework. **(A)** thick-bedded dark-grey dolomudstone-thin-bedded spotted thrombolite; **(B)** thick-bedded dark-grey dolomudstone-thin-bedded dark-grey wavy stromatolite; **(C)** thick-bedded dark-grey dolomudstone-thin-bedded layered thrombolite; **(D)** thin-bedded dark-grey dolomudstone-thick-bedded spotted thrombolite; **(E)** thick-bedded spotted thrombolite-dolograinstone; **(F)** thin-medium-bedded light-grey wavy stromatolite-light-grey dolomudstone; **(G)** thin-medium-bedded dark-grey dolomudstone-layered thrombolite-wavy stromatolite; **(H)** thin-medium-bedded dolopackstone-light-grey wavy stromatolite-light-grey dolomudstone; **(I)** thin-bedded layered thrombolite-wavy stromatolite-light-grey dolomudstone.

generally low, ranging from 0.425 ppm to 3.393 ppm (mean value = 1.697 ppm). The Y/Ho ratios are between 25.652 and 90.611 (mean value = 46.306).

4.3.2 REE anomalies

The equations by Lawrence et al. (2006) are selected to calculate the La, Ce and Eu anomalies: $(La/La^*)_{SN} = La_{SN}/(Pr_{SN}(Pr_{SN}/Nd_{SN})^2)$; $(Ce/Ce^*)_{SN} = Ce_{SN}/(Pr_{SN}(Pr_{SN}/Nd_{SN}))$; $(Eu/Eu^*)_{SN} = Eu_{SN}/(Sm_{SN}^2 Tb_{SN})^{1/3}$. The calculated $(La/La^*)_{SN}$ values are between 0.478 and 2.635 (mean value = 1.241); $(Ce/Ce^*)_{SN}$ values range from 0.554 to 1.501 (mean value = 0.919); and the $(Eu/Eu^*)_{SN}$ values range from 0.371 to 1.884 (mean value = 1.136) (Table 2).

4.3.3 Carbon and oxygen isotopes

The $\delta^{13}C$ and $\delta^{18}O$ values of the studied matrix dolostone samples are summarized in Table 3. The $\delta^{13}C$ values range from −0.860‰ to 3.150‰. And the $\delta^{18}O$ values range from −8.990‰ to −3.450‰.

5 Discussion

5.1 Depositional evolution of microbialite lithofacies associations

5.1.1 Lithofacies associations distribution during late fourth-order TST—early fourth-order HST

Compared with individual lithofacies, lithofacies associations better indicate specific depositional settings of various microbialites in different areas of the rimmed carbonate platform within a fourth-order depositional sequence. The overall dark color and the frequent occurrence of thick-bedded dark-grey dolomudstone in Lithofacies Associations A, B and C suggest low-energy settings. The scattered clots of spotted thrombolites imply a deeper and moderate-energy sub-tidal setting, with enough accommodation (Aitken, 1967; Riding, 2011). Therefore, the combination of thick-bedded dark-grey dolomudstone with thin-bedded spotted thrombolite (Lithofacies Association A) suggests a low-moderate-energy sub-tidal setting in the platform margin, where small-scaled spotted thrombolitic reefs occur. The dark color, dense laminae and the dark-grey microcrystalline cements of dark-grey wavy stromatolites might indicate their main distribution in a relatively tranquil environment in the platform interior. The layered thrombolite, also termed as "composite microbialite" by Harwood and Summer (2011), is characterized by intermingled clotted and laminated textures at a sub-centimeter scale. The layered densely-packed clots indicate their development with energy between that of spotted thrombolites and wavy stromatolites. Lithofacies Associations B (thick-bedded dark-grey dolomudstone - thin-bedded dark-grey wavy stromatolite) and C (thick-bedded dark-grey dolomudstone - thin-bedded layered thrombolite) thus suggest low-energy settings of platform interior, such as lagoonal environments, where small-scaled dark wavy stromatolitic reefs and small-scaled layered thrombolitic reefs occasionally develop.

5.1.2 Lithofacies associations distribution during late fourth-order HST—next early fourth-order TST

From late HST of fourth-order sequence to the early TST of the next, lithofacies associations are more diverse. Lithofacies Associations D, E and F are flourished in platform margin. The thick-bedded spotted thrombolites of Lithofacies Associations D and E imply that their corresponding settings are suitable for the development of large-scaled spotted thrombolitic reefs. Compared with Lithofacies

TABLE 1 Al content (%), trace element concentrations (ppm) and ratios of the studied samples (LFA, lithofacies association).

Sample no.	Depth	Lithology	LFA	Al	Th	Zr	Sc	V	Ni	Sr	Ba	U	Nd	Sr/Ba	Ba/Nd	Mn/Sr
MX105-1	5303.30	Dolograinstone	E	0.106	0.073	0.397	0.067	2.838	0.620	107.988	52.570	0.073	0.233	2.054	225.414	1.388
MX105-2	5308.28	Dolograinstone	E	0.069	0.014	0.014	0.025	1.356	0.471	38.826	14.320	0.014	0.611	2.711	23.423	6.588
MX105-3	5325.00	Dolograinstone	E	0.006	0.031	3.094	0.044	2.862	0.037	23.630	8.140	0.031	0.143	2.903	56.881	4.311
MX105-4	5349.50	Spotted thrombolite	A/D	0.138	0.055	1.690	0.049	2.119	0.086	35.616	29.599	0.055	0.437	1.203	67.799	3.812
MX105-5	5357.38	Light-grey dolomudstone	F	0.011	0.037	0.376	0.017	4.936	2.152	67.170	98.839	0.037	0.340	0.680	290.516	4.752
MX51-1	5335.80	Light-grey wavy stromatolite	I	0.016	0.028	0.598	0.052	0.052	0.213	44.825	36.800	0.486	0.332	1.218	110.944	8.083
MX51-2	5342.00	Layered thrombolite	G	0.027	0.036	0.375	0.035	0.035	0.271	63.219	14.384	0.520	0.204	4.395	70.410	1.324
MX51-3	5347.06	Light-grey dolomudstone	I	0.001	0.035	0.243	0.029	0.029	1.623	78.123	36.204	0.279	0.599	2.158	60.446	6.231
MX51-4	5351.69	Light-grey wavy stromatolite	H	0.001	0.010	0.050	0.016	0.016	0.425	62.961	22.518	0.606	0.121	2.796	186.795	2.239
MX51-5	5368.52	Layered thrombolite	G	0.011	0.015	0.322	0.006	0.006	0.894	37.703	5.598	0.273	0.250	6.735	22.379	10.667
MX51-6	5395.16	Layered thrombolite	C	0.328	0.009	0.629	0.000	0.000	0.385	31.230	6.902	0.433	0.147	4.525	47.080	1.305
MX39-1	5277.74	Layered thrombolite	G	0.064	0.069	0.883	0.337	15.432	15.400	40.722	6.318	0.138	0.380	6.445	16.635	4.357
MX39-2	5292.72	Layered thrombolite	G	0.002	0.006	0.038	0.024	7.982	7.980	42.696	16.293	0.809	0.066	2.620	245.760	4.671
GS20-1	5206.82	Light-grey dolomudstone	I	0.011	0.024	0.108	0.174	5.522	0.527	55.585	22.777	0.195	0.591	2.440	38.515	9.972
GS20-2	5220.28	Dolopackstone	H	0.021	0.020	0.590	0.049	2.446	0.635	78.895	61.810	0.865	0.674	1.276	91.760	4.074
GS20-3	5255.13	Light-grey dolomudstone	I	0.008	0.038	0.173	0.120	1.643	0.386	50.482	35.050	0.194	0.546	1.440	64.169	2.042
GS20-4	5261.27	Layered thrombolite	C	0.016	0.006	0.134	0.008	6.169	0.134	51.685	35.155	0.135	0.273	1.470	128.895	6.982
GS21-1	5265.81	Dark-grey wavy stromatolite	B	0.010	0.021	0.029	0.083	7.086	0.020	30.882	8.535	0.142	0.278	3.618	0.276	23.091
GS21-2	5284.00	Light-grey wavy stromatolite	H	0.170	0.018	0.312	0.086	9.493	1.288	39.184	4.232	1.070	0.602	9.258	0.103	15.313
GS21-3	5289.39	Dolopackstone	H	0.016	0.016	0.028	0.030	10.872	0.330	81.474	19.442	0.279	0.253	4.191	0.359	3.785
GS21-4	5293.63	Light-grey wavy stromatolite	H	0.042	0.014	0.033	0.013	4.203	0.075	39.872	4.966	0.348	0.323	8.030	0.309	13.571
GS21-5	5304.02	Dark-grey wavy stromatolite	B	0.016	0.010	0.139	0.037	2.926	0.400	48.936	5.807	0.477	0.225	8.428	0.163	7.971
GS21-6	5313.36	Layered thrombolite	G	0.007	0.013	0.156	0.014	1.428	0.306	54.696	8.035	0.247	0.179	6.807	0.560	1.521

10.3389/feart.2023.1085313

10.3389/feart.2023.1085313

TABLE 2 REE+Y concentrations, ratios and anomalies of the studied samples (ppm) (LFA, lithofacies association; SN, shale normalized).

Sample No.	Depth	Lithology	LFA	La	Ce	Pr	Nd	Sm	Eu	Gd	Tb	Dy	Ho	Er	Tm	Yb	Lu	Y	∑REE	Y/Ho	Dy_N/Sm_N	$(La/La^*)_{SN}$	$(Ce/Ce^*)_{SN}$	$(Eu/Eu^*)_{SN}$
MX105-1	5303.30	Dolograinstone	E	0.323	0.648	0.067	0.233	0.061	0.011	0.044	0.008	0.055	0.005	0.016	0.008	0.033	0.005	0.296	1.519	57.320	1.164	1.042	1.030	0.964
MX105-2	5308.28	Dolograinstone	E	0.469	1.079	0.140	0.611	0.080	0.038	0.211	0.023	0.165	0.039	0.101	0.010	0.047	0.005	1.254	3.019	31.797	2.622	1.154	1.040	1.884
MX105-3	5325.00	Dolograinstone	E	0.147	0.233	0.036	0.143	0.032	0.011	0.043	0.008	0.048	0.007	0.041	0.006	0.037	0.003	0.621	0.795	90.611	1.886	1.163	0.792	1.405
MX105-4	5349.50	Spotted thrombolite	A/D	0.331	0.556	0.094	0.437	0.075	0.016	0.154	0.015	0.112	0.021	0.038	0.005	0.029	0.004	0.868	1.886	40.846	1.901	1.374	0.849	0.975
MX105-5	5357.38	Light-grey dolomudstone	F	0.303	0.552	0.062	0.340	0.071	0.027	0.130	0.016	0.063	0.014	0.022	0.006	0.056	0.003	0.613	1.666	43.473	1.125	2.635	1.501	1.613
MX51-1	5335.80	Light-grey wavy stromatolite	I	0.468	0.747	0.077	0.332	0.072	0.016	0.067	0.005	0.039	0.009	0.024	0.005	0.016	0.002	0.475	1.879	50.241	0.687	2.019	1.283	1.429
MX51-2	5342.00	Layered thrombolite	G	0.250	0.477	0.052	0.204	0.031	0.011	0.054	0.007	0.042	0.010	0.023	0.003	0.013	0.002	0.315	1.178	32.586	1.732	1.309	1.096	1.522
MX51-3	5347.06	Light-grey dolomudstone	I	0.608	1.225	0.168	0.599	0.142	0.028	0.191	0.031	0.188	0.039	0.099	0.014	0.055	0.007	1.106	3.393	28.503	1.690	0.836	0.806	0.876
MX51-4	5351.69	Light-grey wavy stromatolite	H	0.148	0.249	0.027	0.121	0.040	0.009	0.018	0.005	0.037	0.006	0.012	0.002	0.018	0.002	0.221	0.694	36.759	1.176	1.874	1.229	1.225
MX51-5	5368.52	Layered thrombolite	G	0.240	0.515	0.072	0.250	0.053	0.017	0.092	0.012	0.097	0.013	0.047	0.006	0.025	0.000	0.501	1.439	37.594	2.329	0.744	0.778	1.361
MX51-6	5395.16	Layered thrombolite	C	0.133	0.280	0.048	0.147	0.042	0.004	0.040	0.013	0.081	0.017	0.082	0.009	0.090	0.006	0.563	0.990	32.334	2.472	0.478	0.559	0.371
MX39-1	5277.74	Layered thrombolite	G	0.623	1.121	0.118	0.380	0.078	0.017	0.098	0.006	0.082	0.025	0.068	0.006	0.037	0.011	0.788	2.670	31.356	1.336	0.990	0.945	1.348
MX39-2	5292.72	Layered thrombolite	G	0.101	0.155	0.019	0.066	0.025	0.006	0.008	0.007	0.017	0.006	0.013	0.001	0.000	0.001	0.144	0.425	25.652	0.881	1.181	0.887	0.916
GS20-1	5206.82	Light-grey dolomudstone	I	0.506	0.936	0.150	0.591	0.114	0.019	0.121	0.028	0.076	0.013	0.044	0.007	0.021	0.010	0.818	2.636	64.923	0.857	0.959	0.766	0.711
GS20-2	5220.28	Dolopackstone	H	0.514	1.066	0.146	0.674	0.087	0.036	0.112	0.014	0.038	0.011	0.018	0.004	0.000	0.003	0.626	2.722	54.631	0.551	1.353	1.040	1.991
GS20-3	5255.13	Light-grey dolomudstone	I	0.396	0.772	0.120	0.546	0.069	0.020	0.089	0.042	0.025	0.009	0.025	0.005	0.000	0.001	0.460	2.120	50.023	0.469	1.249	0.910	0.908
GS20-4	5261.27	Layered thrombolite	C	0.279	0.442	0.070	0.273	0.073	0.009	0.069	0.009	0.078	0.007	0.028	0.002	0.022	0.004	0.428	1.363	64.804	1.360	1.101	0.764	0.673
GS21-1	5265.81	Dark-grey wavy stromatolite	B	0.289	0.507	0.064	0.278	0.057	0.013	0.077	0.009	0.035	0.010	0.032	0.000	0.024	0.004	0.480	1.399	47.974	0.786	1.526	1.056	1.101
GS21-2	5284.00	Light-grey wavy stromatolite	H	0.548	0.923	0.142	0.602	0.152	0.026	0.134	0.016	0.126	0.025	0.054	0.005	0.044	0.004	0.975	2.799	39.587	1.055	1.257	0.853	0.972
GS21-3	5289.39	Dolopackstone	H	0.262	0.394	0.065	0.253	0.040	0.007	0.051	0.007	0.035	0.005	0.019	0.008	0.009	0.003	0.395	1.159	73.605	1.107	1.105	0.730	0.872
GS21-4	5293.63	Light-grey wavy stromatolite	H	0.239	0.387	0.064	0.323	0.063	0.011	0.070	0.009	0.054	0.010	0.020	0.004	0.014	0.004	0.395	1.271	40.928	1.089	1.743	0.952	0.852
GS21-5	5304.02	Dark-grey wavy stromatolite	B	0.200	0.419	0.064	0.225	0.058	0.015	0.091	0.007	0.029	0.014	0.012	0.002	0.016	0.003	0.469	1.155	33.687	0.633	0.713	0.723	1.394
GS21-6	5313.36	Layered thrombolite	G	0.179	0.270	0.052	0.179	0.036	0.006	0.034	0.006	0.040	0.004	0.029	0.002	0.011	0.004	0.215	0.852	55.810	1.402	0.740	0.554	0.756

Association E, Lithofacies Association D (thin-bedded dark-grey dolomudstone—thick-bedded spotted thrombolite) indicates a moderate-high-energy shallow subtidal setting closer to the open sea, where large-scaled spotted thrombolitic reefs develop. The moderate-well-sorted sub-rounded to rounded grains in dolograinstones of Lithofacies Association E (thick-bedded spotted thrombolite—dolograinstone) imply strong water agitation (Lan et al., 2022a), whose setting can be interpreted as a high-energy zone that favors the co-occurrence of large-scaled spotted thrombolitic reefs and shoals. In most cases, the light color, loose laminae, bright-colored microcrystalline cements and occasional bird-eye structures of light-grey wavy stromatolites indicate their development in a shallower moderate-low-energy inter-tidal setting in platform interior (Flügel, 2010; Grotzinger and Al-Rawahi, 2014). In Lithofacies Association F (thin-medium-bedded light-grey wavy stromatolite—light-grey dolomudstone), a few light-grey wavy stromatolites are observed, which might correspond to moderate—low energy areas closer to platform interior in platform margin.

In the mean time, Lithofacies Associations G, H and I are distributed in platform interior. Lithofacies Association G (thin-medium-bedded dark-grey dolomudstone—layered thrombolite—light-grey wavy stromatolite) is the most developed lithofacies association in platform interior, corresponding to a low-moderate energy subtidal-intertidal shallow lagoonal environment where layered thrombolitic and wavy stromatolitic "patch reefs" flourish. The smaller-sized peloids and microbial fragments in dolopackstones of Lithofacies Association H (thin-medium-bedded dolopackstone—light-grey wavy stromatolite—light-grey dolomudstone) may suggest a high-energy setting with co-occurrence of wavy stromatolitic reefs and shoals (Lan et al., 2022a). The light color, few microbial fabrics and the frequently-occurred bird-eye structures of Lithofacies Association L (thin-bedded layered thrombolite—light-grey wavy stromatolite—light-grey dolomudstone) indicate a frequently exposed low-energy intertidal - supratidal setting in platform interior, where microbialites are less developed.

5.2 Environmental constraints of the microbialites

5.2.1 Geochemical data reliability analysis

Terrigenous input likely alters the depositional archives of ancient carbonates, especially the Precambrian samples (Tostevin et al., 2016; Hood et al., 2018), which should be carefully screened before they are analyzed for paleo-environment reconstruction. According to previous studies (Bau et al., 1997; Webb and Kamber, 2000; Ling et al., 2013; Wang et al., 2020; Lan et al., 2022b), the REE + Y data can preserve the paleo-environmental significance if Al < 0.35%, Zr < 4.00 ppm, Th < 0.10 ppm, Sc <1.00 ppm, and ∑REE <4.00 ppm. The maximum Al, Th, Zr, Sc and ∑REE concentrations of the studied samples are respectively 0.328%, 0.073 ppm, 3.094 ppm, 0.337 ppm and 3.393 ppm, which are below the thresholds above. Additionally, the Al, Th, Zr, Sc and ∑REE concentrations have little correlation with each other (Figures 7A–J), reinforcing that the samples are free from terrigenous contamination. The PAAS normalized REE + Y patterns of the samples are close to those of modern seawater and average Holocene microbialite (Webb and Kamber, 2000) rather than the hydrothermal dolomites (Nutman et al., 2010), showing that the REE + Y data are reliable for paleo-environmental analysis (Figure 8).

Diagenetic modifications may also affect the original depositional signatures of the geochemistry proxies. Although the REE in carbonates are relatively stable during diagenesis, the later fluid exchange could result in Ce enrichment, Eu deficiency and low Dy_N/Sm_N ratios and weakened REE + Y patterns with seawater signatures, which could be shown as negative correlations of $(Ce/Ce^*)_{SN}$ and $(Eu/Eu^*)_{SN}$ with Dy_N/Sm_N (Shields and Stille, 2001). The little correlation of Ba/Nd with $(Eu/Eu^*)_{SN}$, $(Eu/Eu^*)_{SN}$ with $(Ce/Ce^*)_{SN}$, and Dy_N/Sm_N with $(Ce/Ce^*)_{SN}$ indicates that the REE + Y data are not diagenetically altered (Figure 9). Moreover, if the Mn/Sr ratios of samples are less than 10 and the $\delta^{13}C$ and $\delta^{18}O$ values are not correlated, the carbon and oxygen isotope values can be applied for depositional paleo-environment analysis (Derry et al., 1994; Kaufman and Knoll, 1995). There are four samples with Mn/Sr ratios greater than 10, which have been screened out. The $\delta^{13}C$ and $\delta^{18}O$ values of the remaining samples are not correlated (Figure 9), ensuring that they preserve their paleo-environmental record (Figure 10).

5.2.2 Paleo-salinity and redox analysis

The Sr/Ba ratio has been widely regarded as a paleo-salinity indicator for both marine and continental sediments: under low-salinity conditions, Sr and Ba occur in the forms of oxides, sulfides or soluble bicarbonates; when salinity increases to a threshold, Ba precipitates prior in the form of $BaSO_4$, resulting in greater Sr/Ba ratios; if salinity increases continuously, Sr would precipitate in the form of $SrSO_4$ (Paytan et al., 2007; Adegoke et al., 2014; Stüeken et al., 2020; Wei and Algeo, 2020). Therefore Sr/Ba ratios are positively correlated with paleo-salinity (Wei et al., 2021), and their ranges for freshwater, brackish and marine facies are <0.2, 0.2–0.5 and >0.5, respectively (Wei and Algeo, 2020). Recently, the Sr/Ba ratio has been adopted for paleo-salinity analysis of Ediacaran and early Cambrian marine carbonates, including microbialites (Yang et al., 2021; Rodrigues et al., 2022; Sun et al., 2022; Zhang and Zheng, 2022; Zheng et al., 2022). The Sr/Ba ratios of the screened samples range from 0.680 to 8.428, which are all greater than 0.5, showing their marine origin. The platform margin lithofacies associations (A, D, E, F) are characterized by Sr/Ba ratios between 0.680 and 2.903 (mean value = 1.910); while the Sr/Ba ratios of the platform interior lithofacies associations (B, C, G, H, I) are between 1.218 and 8.428 (mean value = 3.586), indicating higher seawater salinity of platform interior (Figure 11A). Lithofacies Associations B, C and G (layered thrombolite and wavy stromatolite enriched) are characterized by higher mean Sr/Ba ratios than the remaining lithofacies associations (spotted thrombolites or non-microbialites dominated) (Figure 11B). Specifically, the mean Sr/Ba ratio (4.301) of layered thrombolite and wavy stromatolite lithofacies is higher than that of other lithofacies (2.106), which may suggest high-salinity and more restricted settings for platform interior layered thrombolites and wavy stromatolites. Recent studies of terminal Ediacaran microbialites in peripheral Sichuan Basin (Lin et al., 2017); Li et al. (2022) also reveal greater mean Sr/Ba ratios of laminated microbialites than those of non-laminated microbialites, which is in accordance with this study.

Besides Sr/Ba ratios, previous studies indicate that carbon and oxygen isotopes of marine carbonates can also reflect seawater salinity: the $\delta^{13}C$ and $\delta^{18}O$ values are positively correlated with

TABLE 3 $\delta^{13}C$ and $\delta^{18}O$ values of the studied samples with Mn/Sr ratios <10 (LFA, lithofacies association).

Sample No.	Depth	Lithology	LFA	$\delta^{13}C$	$\delta^{18}O$
MX105-1	5303.30	Dolograinstone	E	2.520	−8.990
MX105-2	5308.28	Dolograinstone	E	0.680	−8.730
MX105-3	5325.00	Dolograinstone	E	2.340	−5.620
MX105-4	5349.50	Spotted thrombolite	A/D	2.610	−6.400
MX105-5	5357.38	Light-grey dolomudstone	F	1.530	−4.800
MX51-1	5335.80	Light-grey wavy stromatolite	I	0.680	−7.060
MX51-2	5342.00	Layered thrombolite	G	0.850	−6.810
MX51-3	5347.06	Light-grey dolomudstone	I	1.180	−4.720
MX51-4	5351.69	Light-grey wavy stromatolite	H	−0.860	−6.550
MX51-6	5395.16	Layered thrombolite	C	3.150	−3.450
MX39-1	5277.74	Layered thrombolite	G	1.500	−4.370
MX39-2	5292.72	Layered thrombolite	G	1.400	−5.100
GS20-1	5206.82	Light-grey dolomudstone	I	1.420	−6.710
GS20-2	5220.28	Dolopackstone	H	1.710	−6.420
GS20-3	5255.13	Light-grey dolomudstone	I	2.810	−6.250
GS20-4	5261.27	Layered thrombolite	C	2.930	−6.250
GS21-3	5289.39	Dolopackstone	H	1.310	−5.370
GS21-5	5304.02	Dark-grey wavy stromatolite	B	1.070	-5.610
GS21-6	5313.36	Layered thrombolite	G	2.090	-3.850

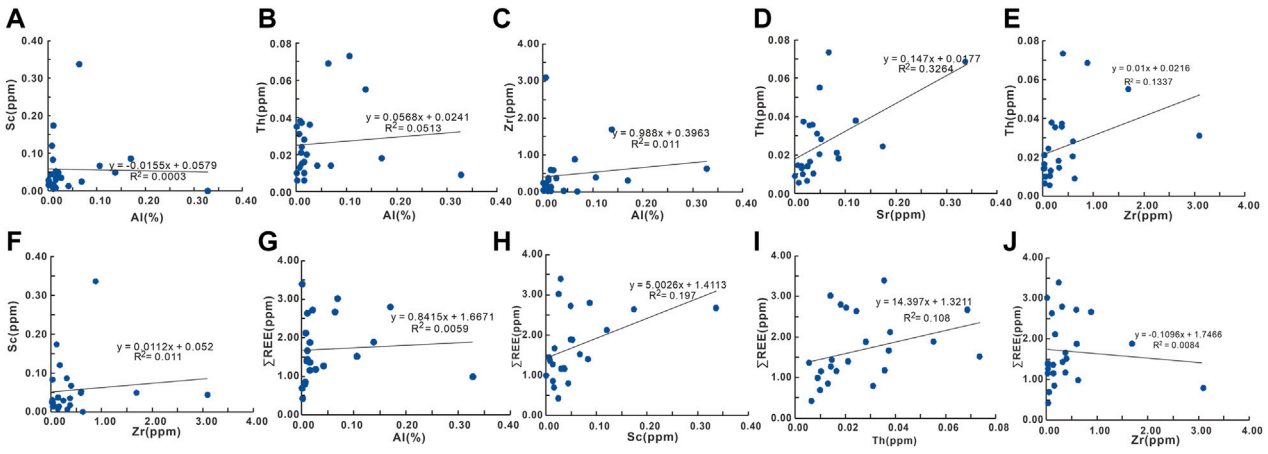

FIGURE 7
Cross-plots showing the concentration correlations of **(A)** Al and Sc; **(B)** Al and Th; **(C)** Al and Zr; **(D)** Sc and Th; **(E)** Zr and Th; **(F)** Zr and Sc; **(G)** Al and ∑REE; **(H)** Sc and ∑REE; **(I)** Th and ∑REE; **(J)** Zr and ∑REE.

paleo-salinity (Keith and Weber, 1964). The $\delta^{13}C$ values of platform margin lithofacies associations are between 0.680‰ and 2.610‰ (mean value = 1.940‰), while those of platform interior lithofacies associations are between −0.860‰ and 3.150‰ (mean value = 1.517‰) (Figure 11C). The $\delta^{18}O$ values of platform margin lithofacies associations range from −8.990‰ to −4.800‰ (mean value = −6.910‰), while those of the platform interior lithofacies associations range from −7.060‰ to −3.450‰ (mean value = −5.608‰), which may indicate higher salinity of platform interior lithofacies associations (Figure 11D). In addition to salinity comparison, $(La/La^*)_{SN}$ has been used to analyze the restrictiveness of various depositional settings: lower $(La/La^*)_{SN}$

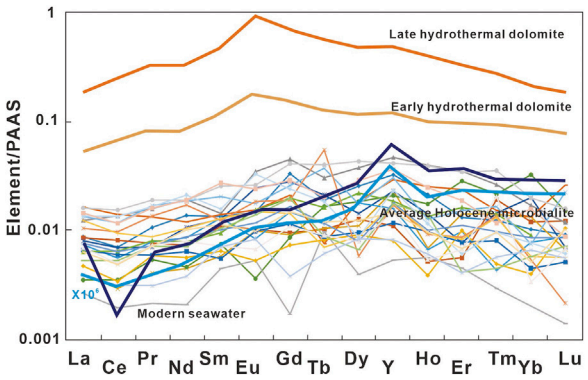

FIGURE 8
PAAS-normalized patterns of REE + Y of matrix dolostones. (The REE +Y patterns of the modern seawater and Holocene microbialites, and hydrothermal dolomites are from Webb and Kamber, 2000; Nutman et al., 2010).

may relate to a more restricted environment (Cai et al., 2022). Study by Eltom et al. (2017) on Ediacaran carbonates also suggested that $(La/La^*)_{SN}$ consistently showed a strong positive anomaly toward the open marine facies compared with peritidal facies. In the studied samples, the $(La/La^*)_{SN}$ values of platform margin lithofacies associations are between 1.042 and 2.635 (mean value = 1.474), while those of platform interior lithofacies associations are between 0.478 and 2.019 (mean value = 1.136) (Figure 11E), which may imply a more restricted setting of the platform interior layered thrombolite and wavy stromatolite enriched lithofacies associations.

The $(Ce/Ce^*)_{SN}$ value is an efficient proxy for redox analysis of marine carbonate depositional environments (Bau and Dulski, 1996; Ling et al., 2013; Hood and Wallace, 2015). Under oxic conditions, soluble Ce^{3+} would be oxidized into Ce^{4+} and be absorbed on the surface of Fe or Mn hydroxides, resulting in Ce deficient in seawater relative to other rare earth elements (German and Elderfield, 1990). Therefore a negative Ce anomaly might indicate oxic conditions (with $(Ce/Ce^*)_{SN}$ values of 0.06–0.16 for modern oxygenated oceans (Byrne and Sholkovitz, 1996; Ling et al., 2013), while the absence of negative Ce anomaly may suggest sub-oxic or anoxic conditions (Lawrence et al., 2006). The $(Ce/Ce^*)_{SN}$ values of the studied samples range from 0.554 to 1.501. The $(Ce/Ce^*)_{SN}$ values of the platform margin lithofacies associations are between 0.792 and 1.501 (mean value = 1.043); while those of the platform interior lithofacies associations are between 0.554 and 1.283 (mean value = 0.878), showing that the platform interior might be more oxygenated. However, compared with the distinct Sr/Ba value variation of individual lithofacies association, the $(Ce/Ce^*)_{SN}$ values are less varied. Nevertheless, for individual microbialite lithofacies, the mean $(Ce/Ce^*)_{SN}$ value of wavy stromatolites (1.078) is higher than that of layered thrombolites (0.801) and spotted thrombolites (0.849). (Figure 11F).

5.3 Depositional—paleo-environmental evolution of terminal Ediacaran microbialites with environmental and reservoir implications

5.3.1 A depositional—paleo-environmental evolution model

Combing the depositional distribution of the microbialite lithofacies associations with salinity and redox characteristics, a depositional - environmental evolution model for the microbialites within a fourth-order sequence of the Gaoshiti—Moxi area is established (Figure 12). From late TST to early HST, small-scaled spotted thrombolitic reefs are distributed in the low-salinity and more oxygenated sub-tidal zone of platform margin; while small-scaled dark wavy stromatolitic reefs and layered thrombolitic reefs are distributed in high-salinity and less oxygenated relatively deep lagoonal enviroments in platform interior (Figure 12A). From late HST to early TST of the next fourth-order sequence, the microbialites are more developed. In the platform margin, large-scaled spotted thrombolitic reefs are distributed in a shallow sub-tidal setting towards the open sea, thrombolitic reef—shoal complexes are distributed in the high-energy zone, and small-medium-scaled stromatolitic reefs are distributed in the inter-tidal zone close to the platform interior; all are characterized by low-salinity and less oxygenation. In the platform interior, layered thrombolitic reefs and wavy stromatolitic reefs are distributed in high-salinity and less oxygenated deep sub-tidal—shallower inter-tidal lagoons, wavy stromatolitic

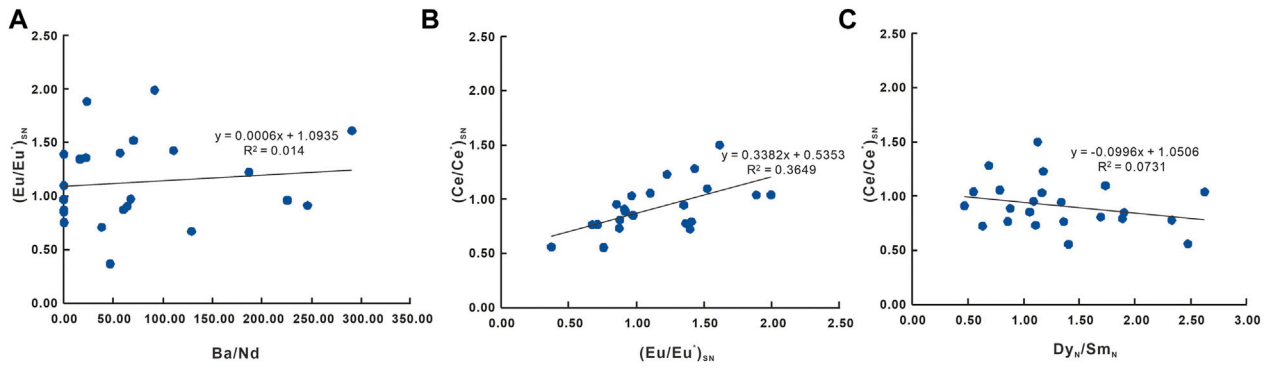

FIGURE 9
Cross-plots showing the correlations of **(A)** Ba/Nd and $(Eu/Eu^*)_{SN}$ values; **(B)** $(Eu/Eu^*)_{SN}$ and $(Ce/Ce^*)_{SN}$ values; and **(C)** Dy_N/Sm_N and $(Ce/Ce^*)_{SN}$.

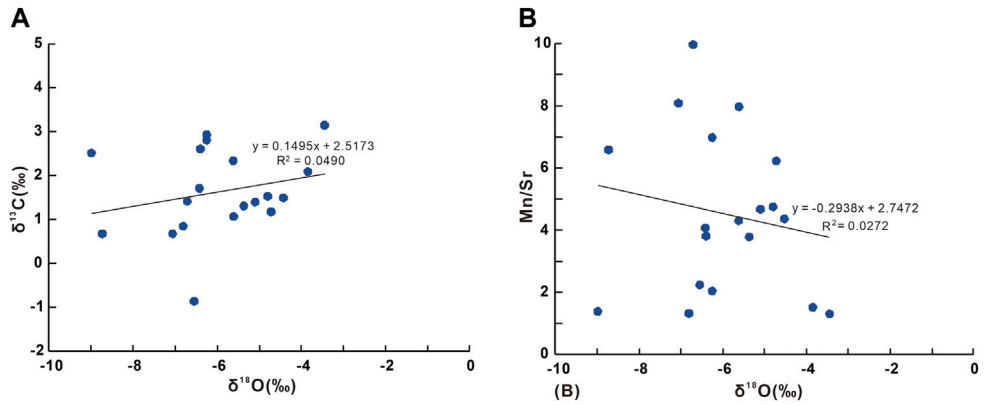

FIGURE 10
Cross-plots showing the correlations of **(A)** $\delta^{18}O$ and $\delta^{13}C$ values and **(B)** $\delta^{18}O$ values and Mn/Sr ratios.

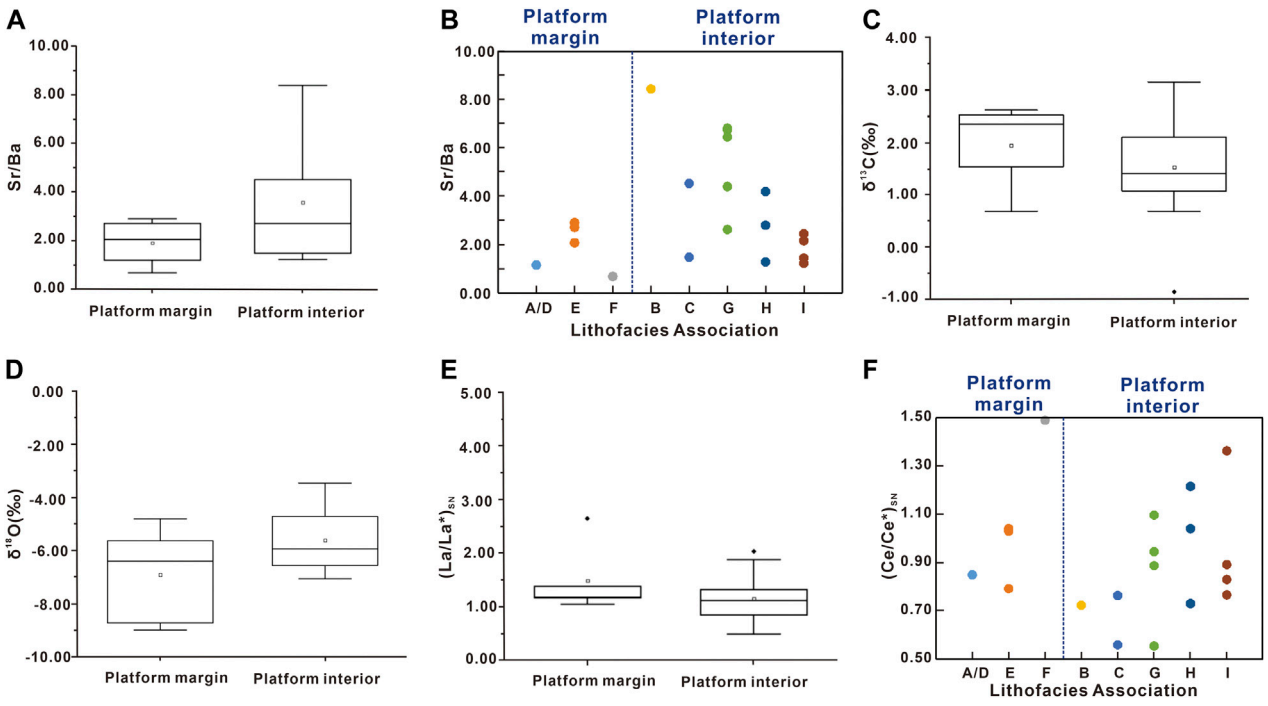

FIGURE 11
Salinity and redox related geochemical proxies characteristics of different microbialite lithofacies associations. **(A)** Box plot of the Sr/Ba ratios of microbialite lithofacies associations in platform margin and platform interior. **(B)** Sr/Ba ratios of individual microbialite lithofacies association. **(C)** Box plot of $\delta^{13}C$ values of microbialite lithofacies associations in platform margin and platform interior. **(D)** Box plot of $\delta^{18}O$ values of microbialite lithofacies associations in platform margin and platform interior. **(E)** $(La/La^*)_{SN}$ values of microbialite lithofacies associations in platform margin and platform interior. **(F)** $(Ce/Ce^*)_{SN}$ values of individual microbialite lithofacies association.

reef—shoal complexes are distributed in moderate-salinity and more oxgenated high-energy zone in inter-tidal areas and supra-tidal flats. Specifically, when fourth-order sea level falls, the platform interior develops various "micro-environments" with overall high salinity but diverse redox conditions; among all the lithofacies, the layered thrombolites and wavy stromatolites are characterized with the highest salinity and more reduced redox state (Figure 12B).

5.3.2 Implication for environmental constraints of terminal Ediacaran microbialites and seawater chemistry

More and more attention has been paid on paleo-environmental factors such as salinity and redox in the study of Precambrian microbialite-dominated depositional systems (Oliveri et al., 2010; Husinec, 2016; Chen et al., 2021). The paleo-environmental analysis of the studied samples suggests that during terminal Ediacaran

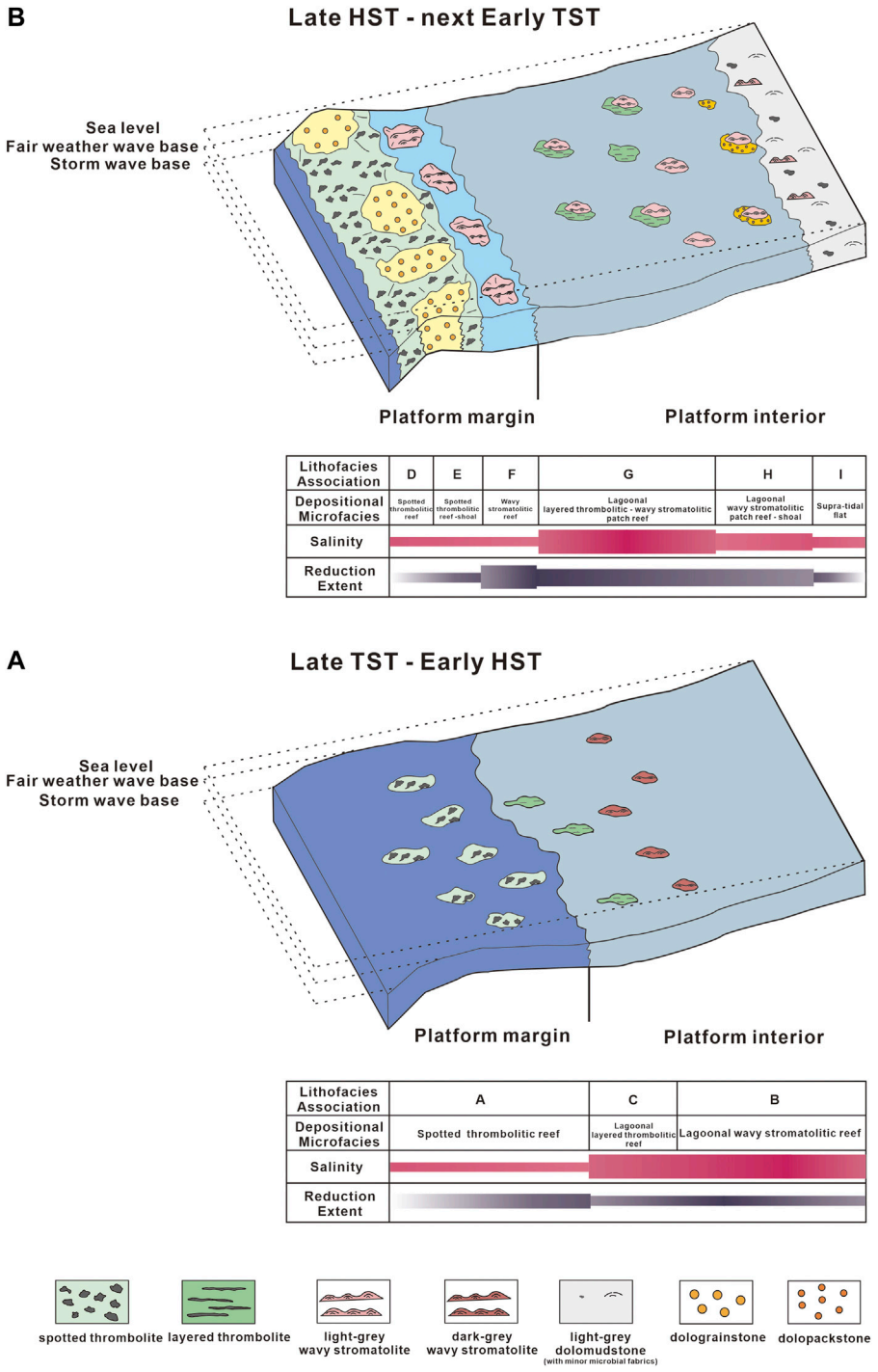

FIGURE 12
Depositional-paleo-environmental model of the microbialites of Z_2dn^4 in a fourth-order sequence stratigraphic framework of the Gaoshiti—Moxi area. **(A)** Depositional-paleo-environmental evolution model of the microbialites during late fourth-order TST-early fourth-order HST. **(B)** Depositional-paleo-environmental model of the microbialites during late fourth-order HST-next early fourth-order TST.

salinity variation occurred in different microbialite lithofacies and lithofacies associations on a rimmed carbonate platform: spotted thrombolites and related lithofacies associations developed in low-salinity settings in platform margin; while layered thrombolites and wavy stromatolites and related lithofacies associations developed in high-salinity settings in platform interior. Furthermore, compared with non-microbialites, the overall salinity of microbialites was higher. The results are in accordance with recent studies suggesting that stromatolites were more tolerant to terminal Ediacaran high-salinity seawater and microbialite types have also varied with salinity changes (Zhang X. et al., 2014; Zhu et al., 2021; Zhu et al., 2022).

Although we also attempted to characterize the redox variation of different microbialite lithofacies and lithofacies associations, the redox variation is less distinct than expected. Our results only suggest that the wavy stromatolites and related lithofacies associations are more reduced than the remaining types, and the overall platform interior might be more oxygenated than platform margin. The redox condition of our studied samples may also help to estimate the shallow marine redox evolution in South China during terminal Ediacaran, which is still controversial. Recent studies of the sub-tidal and peritidal carbonates in Dengying Formation of peripheral Sichuan Basin suggest a highly spatial-temporal heterogeneous redox condition of the late Ediacaran shallow marine (Chen et al., 2015; Zhang et al., 2018; Ding et al., 2022). According to Ding et al. (2022), most of the $(Ce/Ce^*)_{SN}$ values of these shallow marine carbonates range from 0.62 to 1.25, with the majority of $(Ce/Ce^*)_{SN}$ values >0.8 and a mean value of 0.9, implying low oxygen values; vertically, the Dengying Formation develops four oxygenated intervals with mean $(Ce/Ce^*)_{SN}$ values between 0.62 and 0.8, and $(Ce/Ce^*)_{SN}$ values decrease at E-C boundary. The careful redox studies above are concentrated on shallow marine carbonates from the peripheral Sichuan Basin, while the shallow marine carbonates in the inner basin are paid less attention. Only a few $(Ce/Ce^*)_{SN}$ values of Z_2dn^4 have been published, with $(Ce/Ce^*)_{SN}$ values of 0.67–1.03 (Zhou et al., 2020) or 0.50–0.87 (Gao et al., 2016). Most of the $(Ce/Ce^*)_{SN}$ values of our studied samples are between 0.723 and 1.283 (mean value = 0.930), which also implies less oxygenated state of terminal Ediacaran shallow marine. Specifically, close to the E-C boundary, the samples from the wells in platform interior are characterized by lower $(Ce/Ce^*)_{SN}$ values (0.764,0.766,0.792,0.806), which suggest that oxygenation may have also occurred in the inner Sichuan Basin at the eve of Cambrian Explosion. In the future, the combining salinity—redox study of microbialites during high-frequency sea level fluctuation should be paid more attention.

5.3.3 Reservoir implication

In the past few years, great progresses have been made on the exploration of the Z_2dn^4 in the Dengying Formation of the Gaoshiti—Moxi area, most of which are microbialite-related oil and gas reservoirs (Zou et al., 2014; Hu et al., 2018; Wang et al., 2021). Our high-frequency sequence stratigraphic and paleo-environmental study shows that the scale of platform margin spotted thrombolitic reefs and shoals from late fourth-order HST to next early fourth-order TST is obviously larger than any other microbialite or non-microbialite lithofacies, therefore are the best targets for oil and gas exploration. The smaller-scaled platform interior layered thrombolitic and wavy stromatolitic reefs during late HST of the fourth-order sequence might be taken as potential favorable reservoirs. However, the reservoir characterization in the platform still remains less explicit. In future research, high-frequency sequence stratigraphic study combining salinity and redox analyses should be strengthened in the platform interior, so that the potential favorable microbialite - telated reservoirs would be precisely characterized.

6 Conclusion

1) During terminal Ediacaran, microbialite lithofacies associations were developed on a rimmed platform within a fourth-order sequence stratigraphic framework in the Gaoshti—Moxi area, Central Sichuan Basin, SW China. From late TST to early HST, thin-bedded dark-grey dolomudstone—spotted thrombolite association dominated the platform margin; while thin-bedded dark-grey dolomudstone—dark-grey wavy stromatolite association was distributed in platform interior. From late HST to early TST of the next fourth-order sequence, the platform margin was dominated by thick-bedded spotted thrombolite—dolograinstone association, while the platform interior developed thin-medium-bedded layered thrombolite—light-grey wavy stromatolite association.
2) Based on distribution of microbialite lithofacies associations on the rimmed platform, the depositional evolution of microbialites is defined. From late TST to early HST in a fourth-order sequence, the platform margin developed scattered small-scaled spotted thrombolitic reefs, and the platform interior developed small-scaled wavy stromatolitic reefs and layered thrombolitic reefs scarcely. From late fourth-order HST to early TST of the next, large-scaled spotted thromboltic reefs and spotted thrombolitic reef—shoal complexes dominated the platform margin; and platform interior develop layered thrombolitic reefs and wavy stromatolitic reefs in deep sub-tidal—shallower inter-tidal lagoons, inter-tidal wavy stromatolitic reef—shoal complex and supra-tidal microbialite-deficient flats.
3) Salinity serves as an important environmental constraint for terminal Ediacaran microbialites, which can clearly differentiate the microbial lithofacies and lithofacies asssociations in platform margin and platform interior. The platform interior layered thrombolites and wavy stromatolites and their related lithofacies associations are characterized with higher salinity than the platform margin spotted thrombolite and other non-microbialite related lithofacies associations.
4) Redox cannot precisely characterize the variation of microbialite lithofacies associations within a fourth order depositional sequence. The redox condition of the microbialites in the Gaoshiti—Moxi area indicates that shallow marine during terminal Ediacaran was less oxygenated, and oxygenation may have occurred at the Ediacaran—Cambrian boundary.
5) Large-scaled platform margin spotted thrombolitic reefs and shoals from late fourth-order HST to next early fourth-order TST are considered as ideal oil and gas reservoirs. And the smaller-scaled platform interior layered thrombolitic and wavy stromatolitic reefs might serve as potential favorable reservoirs. Future more detailed high-frequency sequence stratigraphic study combining salinity and redox analyses is advocated for successful reservoir characterization in the platform interior.

Data availability statement

The original contributions presented in the study are included in the article, further inquiries can be directed to the corresponding author.

Author contributions

YZ: Methodology, Validation, Formal analysis, Investigation, Data curation, Writing original draft, Visualization. ZL: Conceptualization, Methodology, Validation, Formal analysis, Writing—review and editing, Supervision, Funding acquisition.

Funding

The study is funded by the Strategic Priority Research Program of the Chinese Academy of Sciences, Grant No. XDA14010201.

Acknowledgments

We are grateful to Fanwei Meng, Valerio Acocella and two reviewers for processing our manuscript and the instructive comments. We are also grateful to Prof. Chunfang Cai and Yongjie Hu for discussions and modifications. Denglin Han, Yunxian Feng and Linbo Wang are thanked for their assist during geochemical analyses.

Conflict of interest

The authors declare that the research was conducted in the absence of any commercial or financial relationships that could be construed as a potential conflict of interest.

Publisher's note

All claims expressed in this article are solely those of the authors and do not necessarily represent those of their affiliated organizations, or those of the publisher, the editors and the reviewers. Any product that may be evaluated in this article, or claim that may be made by its manufacturer, is not guaranteed or endorsed by the publisher.

References

Adegoke, A. K., Abdullah, W. H., Hakimi, M. H., and Yandoka, B. M. S. (2014). Geochemical characterisation of fika Formation in the Chad (bornu) basin, northeastern Nigeria: Implications for depositional environment and tectonic setting. *Appl. Geochem.* 43, 1–12. doi:10.1016/j.apgeochem.2014.01.008

Aitken, J. D. (1967). Classification and environmental significance of cryptalgal limestones and dolomites, with illustrations from the cambrian and ordovician of southwestern alberta. *J. Sediment. Res.* 37, 1163–1178. doi:10.1306/74D7185C-2B21-11D7-8648000102C1865D

Bau, M., and Dulski, P. (1996). Distribution of yttrium and rare-Earth elements in the penge and kuruman iron-formations, transvaal supergroup, South Africa. *Precambrian Res.* 79 (1-2), 37–55. doi:10.1016/0301-9268(95)00087-9

Bau, M., M¨oller, P., and Dulski, P. (1997). Yttrium and lanthanides in eastern Mediterranean seawater and their fractionation during redox-cycling. *Mar. Chem.* 56 (1–2), 123–131. doi:10.1016/S0304-4203(96)00091-6

Burne, R. V., and Moore, L. S. (1987). Microbialites: Organosedimentary deposits of benthic microbial communities. *Palaios* 2, 241–254. doi:10.2307/3514674

Byrne, R. H., and Sholkovitz, E. R. (1996). Chapter 158 Marine chemistry and geochemistry of the lanthanides. *Handb. Phys. Chem. rare earths* 23, 497–593. doi:10.1016/S0168-1273(96)23009-0

Cai, C., Lyons, T. W., Sun, P., Liu, D., Wang, D., Tino, C. J., et al. (2022). Enigmatic super-heavy pyrite formation: Novel mechanistic insights from the aftermath of the Sturtian Snowball Earth. *Geochimica Cosmochimica Acta* 334, 65–82. doi:10.1016/j.gca.2022.07.026

Chen, D., Zhou, X., Fu, Y., Wang, J., and Yan, D. (2015). New U–Pb zircon ages of the Ediacaran–Cambrian boundary strata in South China. *Terra nova.* 27, 62–68. doi:10.1111/ter.12134

Chen, Y., Yan, Z., Ezaki, Y., Adachi, N., and Liu, J. (2021). Rare Earth and yttrium elements (REY) patterns of mesostructures of miaolingian (cambrian) thrombolites at jiulongshan, shandong province, China. *Palaeoworld* 30 (4), 627–642. doi:10.1016/j.palwor.2020.12.007

Condon, D., Zhu, M., Bowring, S., Wang, W., Yang, A., and Jin, Y. (2005). U-Pb ages from the neoproterozoic Doushantuo Formation, China. *Science* 308, 95–98. doi:10.1126/science.1107765

de Oliveira, R. S., Nogueira, A. C. R., Romero, G. R., Truckenbrodt, W., and da Silva Bandeira, J. C. (2019). Ediacaran ramp depositional model of the Tamengo Formation, Brazil. *J. S. Am. Earth Sci.* 96, 102348. doi:10.1016/j.jsames.2019.102348

Della Porta, G., Webb, G. E., and McDonald, I. (2015). REE patterns of microbial carbonate and cements from sinemurian (lower jurassic) siliceous sponge mounds (djebel bou dahar, high atlas, Morocco). *Chem. Geol.* 400, 65–86. doi:10.1016/j.chemgeo.2015.02.010

Derry, L. A., Brasier, M. D., Corfield, R. M., Rozanov, A. Y., and Zhuravlev, A. Y. (1994). Sr and C isotopes in lower cambrian carbonates from the siberian craton: A paleoenvironmental record during the 'cambrian explosion'. *Earth Planet. Sci. Lett.* 128 (3-4), 671–681. doi:10.1016/0012-821X(94)90178-3

Dickson, J. (1966). Carbonate identification and Genesis as revealed by staining. *J. Sediment. Res.* 36, 491–505. doi:10.1306/74D714F6-2B21-11D7-8648000102C1865D

Ding, Y., Chen, D., Zhou, X., Guo, C., Huang, T., and Zhang, G. (2019). Cavity-filling dolomite speleothems and submarine cements in the Ediacaran Dengying microbialites, South China: Responses to high-frequency sea-level fluctuations in an 'aragonite–dolomite sea. *Sedimentology* 66 (6), 2511–2537. doi:10.1111/sed.12605

Ding, Y., Li, Z., Liu, S., Song, J., Zhou, X., Sun, W., et al. (2021). Sequence stratigraphy and tectono-depositional evolution of a late Ediacaran epeiric platform in the upper Yangtze area, South China. *Precambrian Res.* 354, 106077. doi:10.1016/j.precamres.2020.106077

Ding, Y., Sun, W., Liu, S., Xie, J., Tang, D., Zhou, X., et al. (2022). Low oxygen levels with high redox heterogeneity in the late Ediacaran shallow ocean: Constraints from I/(Ca + Mg) and Ce/Ce* of the Dengying Formation, South China. *Geobiology* 20, 790–809. doi:10.1111/gbi.12520

Dunham, R. J. (1962). "Classification of carbonate rocks according to depositional textures," in *Classification of carbonate rocks—a symposium*. Editor W. Ham (Colorado: AAPG Memoir), 108–121. doi:10.1306/M1357

Eltom, H. A., Abdullatif, O. M., Makkawi, M. H., and Eltoum, I. E. A. (2017). Rare Earth element geochemistry of shallow carbonate outcropping strata in Saudi Arabia: Application for depositional environments prediction. *Sediment. Geol.* 348, 51–68. doi:10.1016/j.sedgeo.2016.11.005

Flügel, E. (2010). *Microfacies of carbonate rocks: Analysis, interpretation and application*. Berlin, Heidelberg: Springer, 984.

Gao, P., Liu, G., Jia, C., Young, A., Wang, Z., Wang, T., et al. (2016). Redox variations and organic matter accumulation on the Yangtze carbonate platform during late ediacaran–early cambrian: Constraints from petrology and geochemistry. *Palaeogeogr. Palaeoclimatol. Palaeoecol.* 450, 91–110. doi:10.1016/j.palaeo.2016.02.058

German, C. R., and Elderfield, H. (1990). Application of the Ce anomaly as a paleoredox indicator: The ground rules. *Paleoceanography* 5 (5), 823–833. doi:10.1029/PA005i005p00823

Grotzinger, J., and Al-Rawahi, Z. (2014). Depositional facies and platform architecture of microbialite-dominated carbonate reservoirs, Ediacaran–Cambrian Ara Group, Sultante of Om. *AAPG Bull.* 98, 1453–1494. doi:10.1306/02271412063

Grotzinger, J. P., and James, N. P. (2000). Precambrian carbonates: Evolution of understanding. *SEPM Soc. Sediment. Geol.* 67. doi:10.2110/pec.00.67

Grotzinger, J. P., and Knoll, A. H. (1999). Stromatolites in precambrian carbonates: Evolutionary mileposts or environmental dipsticks? *Annu. Rev. earth Planet. Sci.* 27 (1), 313–358. doi:10.1146/annurev.earth.27.1.313

Guo, Q., Strauss, H., Zhu, M., Zhang, J., Yang, X., Lu, M., et al. (2013). High resolution organic carbon isotope stratigraphy from a slope to basinal setting on the Yangtze Platform, South China: Implications for the Ediacaran–Cambrian transition. *Precambrian Res.* 225, 209–217. doi:10.1016/j.precamres.2011.10.003

Guo, X., Hu, D., Huang, R., Wei, Z., Duan, J., Wei, X., et al. (2020). Deep and ultra-deep natural gas exploration in the Sichuan Basin: Progress and prospect. *Nat. Gas. Ind. B* 7 (5), 419–432. doi:10.1016/j.ngib.2020.05.001

Haq, B., Hardenbol, J., and Vail, P. (1987). Chronology of fluctuating sea levels since the Triassic. *Science* 235 (4793), 1156–1167. doi:10.1126/science.235.4793.1156

Harwood, C. L., and Sumner, D. Y. (2011). Microbialites of the neoproterozoic beck spring dolomite, southern California. *Sedimentology* 58 (6), 1648–1673. doi:10.1111/j.1365-3091.2011.01228.x

Hood, A. V. S., Planavsky, N. J., Wallace, M. W., and Wang, X. (2018). The effects of diagenesis on geochemical paleoredox proxies in sedimentary carbonates. *Geochimica Cosmochimica Acta* 232, 265–287. doi:10.1016/j.gca.2018.04.022

Hood, A. V. S., and Wallace, M. W. (2015). Extreme ocean anoxia during the Late Cryogenian recorded in reefal carbonates of Southern Australia. *Precambrian Res.* 261, 96–111. doi:10.1016/j.precamres.2015.02.008

Hu, M., Gao, D., Wei, G., Yang, W., and Xie, W. (2018). Sequence stratigraphy and facies architecture of a mound-shoal-dominated dolomite reservoir in the late Ediacaran Dengying Formation, central Sichuan Basin, SW China. *Geol. J.* 54 (3), 1653–1671. doi:10.1002/gj.3261

Hu, Y., Cai, C., Pederson, C. L., Liu, D., Jiang, L., He, X., et al. (2020). Dolomitization history and porosity evolution of a giant, deeply buried Ediacaran gas field (Sichuan Basin, China). *Precambrian Res.* 338, 105595. doi:10.1016/j.precamres.2020.105595

Husinec, A. (2016). Sequence stratigraphy of the red river formation, williston basin, USA: Stratigraphic signature of the ordovician katian greenhouse to icehouse transition. *Mar. Petroleum Geol.* 77, 487–506. doi:10.1016/j.marpetgeo.2016.07.003

Jiang, G., Christie-Blick, N., Kaufman, A. J., Banerjee, D. M., and Rai, V. (2003). Carbonate platform growth and cyclicity at a terminal proterozoic passive margin, infra krol Formation and krol Group, lesser himalaya, India. *Sedimentology* 50 (5), 921–952. doi:10.1046/j.1365-3091.2003.00589.x

Jiang, G., Shi, X., Zhang, S., Wang, Y., and Xiao, S. (2011). Stratigraphy and paleogeography of the ediacaran Doushantuo Formation (ca. 635–551 Ma) in South China. *Gondwana Res.* 19 (4), 831–849. doi:10.1016/j.gr.2011.01.006

Kamber, B. S., and Webb, G. E. (2007). Transition metal abundances in microbial carbonate: A pilot study based on *in situ* LA-ICP-MS analysis. *Geobiology* 5 (4), 375–389. doi:10.1111/j.1472-4669.2007.00129.x

Kaufman, A. J., and Knoll, A. H. (1995). Neoproterozoic variations in the C-isotopic composition of seawater: Stratigraphic and biogeochemical implications. *Precambrian Res.* 73 (1-4), 27–49. doi:10.1016/0301-9268(94)00070-8

Keith, M. L., and Weber, J. N. (1964). Carbon and oxygen isotopic composition of selected limestones and fossils. *Geochimica cosmochimica acta* 28 (10-11), 1787–1816. doi:10.1016/0016-7037(64)90022-5

Knauth, L. P. (2005). Temperature and salinity history of the precambrian ocean: Implications for the course of microbial evolution. *Geobiol. Object. concepts, Perspect.* 2005, 53–69. doi:10.1016/B978-0-444-52019-7.50007-3

Lan, C., Xu, Z., Chen, H., Yang, W., Lu, C., Li, P., et al. (2022b). Paleoceanographic reconstruction of the ediacaran Dengying Formation, Sichuan Basin, southwest China: Implications for the origin of precambrian microbial carbonates. *J. Asian Earth Sci.* 236, 105340. doi:10.1016/j.jseaes.2022.105340

Lan, C., Xu, Z., Yang, D., Yang, W., Lu, C., Chen, H., et al. (2022a). Stratigraphy and depositional evolution of the terminal Ediacaran platform in the central to northern Sichuan Basin, Southwest China. *Palaeogeogr. Palaeoclimatol. Palaeoecol.* 601, 111142. doi:10.1016/j.palaeo.2022.111142

Land, L. (1980). "The isotopic and trace element geochemistry of dolomite: The state of the art," in *Concepts and models of dolomitization*. Editors D. H. Zenger, J. B. Dunham, and R. L. Ethington (Tulsa, Oklahoma: SEPM, Special publication), Vol. 28, 87–110. doi:10.2110/pec.80.28.0087

Lawrence, M. G., Greig, A., Collerson, K. D., and Kamber, B. S. (2006). Direct quantification of rare Earth element concentrations in natural waters by ICP-MS. *Appl. Geochem.* 21 (5), 839–848. doi:10.1016/j.apgeochem.2006.02.013

Li, A., Gao, D., Hu, M., Zhao, Y., Zhu, C., and Dai, Y. (2021). Deposition model and main factors controlling depositional processes for microbialites in the fourth member, Dengying Formation, central Sichuan Basin. *Acta Sedimentol. Sin.* 2021, 1–20. (in Chinese with English abstract). doi:10.14027/j.issn.1000-0550.2021.156

Li, F., Deng, J., Kershaw, S., Burne, R., Gong, Q., Tang, H., et al. (2021). Microbialite development through the Ediacaran–Cambrian transition in China: Distribution, characteristics, and paleoceanographic implications. *Glob. Planet. Change* 205, 103586. doi:10.1016/j.gloplacha.2021.103586

Li, K., Song, J., Liu, S., Yang, D., Li, Z., Jin, X., et al. (2022). Element enrichment characteristics and paleoenvironmental significance of microbial rock fabric in late ediacaran strata from the Sichuan Basin. *Acta Sedimentol. Sin.* (in Chinese with English abstract). doi:10.14027/j.issn.1000-0550.2022.042

Li, P. W., Luo, P., Chen, M., Song, J. M., Jing, T. F., and Wang, G. Q. (2015). Characteristics and origin of the Upper Sinian microbial carbonate reservoirs at the northwestern margin of Tarim Basin. *Oil Gas Geol.* 36, 416–428. (in Chinese with English abstract). doi:10.11743/ogg20150310

Li, Y., He, D., Li, D., Li, S., Wo, Y., Li, C., et al. (2020). Ediacaran (Sinian) palaeogeographic reconstruction of the Upper Yangtze area, China, and its tectonic implications. *Int. Geol. Rev.* 62, 1485–1509. doi:10.1080/00206814.2019.1655670

Lin, X., Peng, J., Du, L., Yan, J., and Hou, Z. (2017). Characterization of the microbial dolomite of the upper sinian Dengying Formation in the hanyuan area of sichuan province, China. *Acta Geol. Sinica-English Ed.* 91 (3), 806–821. doi:10.1111/1755-6724.13311

Ling, H., Chen, X., Li, D., Wang, D., Shields-Zhou, G., and Zhu, M. (2013). Cerium anomaly variations in ediacaran–earliest cambrian carbonates from the Yangtze gorges area, South China: Implications for oxygenation of coeval shallow seawater. *Precambrian Res.* 225, 110–127. doi:10.1016/j.precamres.2011.10.011

Liu, J., Li, W., Zhang, B., Zhou, H., Yuan, X., Shan, X., et al. (2015). Sedimentary palaeogeography of the sinian in upper Yangtze region. *J. Palaeogeogr.* 17 (6), 735–753. *(in Chinese with English abstract)*. doi:10.7605/gdlxb.2015.06.061

Liu, Q., Zhu, D., Jin, Z., Liu, C., Zhang, D., and He, Z. (2016). Coupled alteration of hydrothermal fluids and thermal sulfate reduction (TSR) in ancient dolomite reservoirs – an example from Sinian Dengying Formation in Sichuan Basin, southern China. *Precambrian Res.* 285, 39–57. doi:10.1016/j.precamres.2016.09.006

Liu, Y., Hu, Z., Gao, S., Günther, D., Xu, J., Gao, C., et al. (2008a). *In situ* analysis of major and trace elements of anhydrous minerals by LA-ICP-MS without applying an internal standard. *Chem. Geol.* 257 (1-2), 34–43. doi:10.1016/j.chemgeo.2008.08.004

Liu, Y., Hu, Z., Gao, S., Günther, D., Xu, J., Gao, C., et al. (2008b). *In situ* analysis of major and trace elements of anhydrous minerals by LA-ICP-MS without applying an internal standard. *Chem. Geol.* 257 (1-2), 34–43. doi:10.1016/j.chemgeo.2008.08.004

Luo, Y., Tan, X., Zhao, D., Luo, W., Liu, Y., Xiao, D., et al. (2022). Sedimentary characteristics of microbial carbonates in the ediacaran and their geological implications: A case study of the member 4 of Dengying Formation from wellblock MX8, central Sichuan Basin. *J. Palaeogeogr. Chin. Ed.* 24 (2), 278–291. (in Chinese with English abstract). doi:10.7605/gdlxb.2022.02.017

Lyons, T. W., Reinhard, C. T., and Planavsky, N. J. (2014). The rise of oxygen in Earth's early ocean and atmosphere. *Nature* 506 (7488), 307–315. doi:10.1038/nature13068

Ma, Y., Guo, X., Guo, T., Huang, R., Cai, X., and Li, G. (2007). The Puguang gas field: New giant discovery in the mature Sichuan Basin, southwest China. *AAPG Bull.* 91, 627–643. doi:10.1306/11030606062

McLennan, S. (1989). Rare Earth elements in sedimentary rocks: Influence of provenance and sedimentary processes. *Rev. Mineral. Geochem.* 21 (1), 169–200. doi:10.1515/9781501509032-010

Nutman, A. P., Friend, C. R., Bennett, V. C., Wright, D., and Norman, M. D. (2010). ≥3700 Ma pre-metamorphic dolomite formed by microbial mediation in the isua supracrustal belt (W. Greenland): Simple evidence for early life? *Precambrian Res.* 183 (4), 725–737. doi:10.1016/j.precamres.2010.08.006

Oliveri, E., Neri, R., Bellanca, A., and Riding, R. (2010). Carbonate stromatolites from a messinian hypersaline setting in the caltanissetta basin, sicily: Petrographic evidence of microbial activity and related stable isotope and rare Earth element signatures. *Sedimentology* 57 (1), 142–161. doi:10.1111/j.1365-3091.2009.01094.x

Paytan, A., Averyt, K., Faul, K., Gray, E., and Thomas, E. (2007). Barite accumulation, ocean productivity, and Sr/Ba in barite across the paleocene–eocene thermal maximum. *Geology* 35 (12), 1139–1142. doi:10.1130/G24162A.1

Peng, H., Ma, K., Zhang, X., Wen, L., Wang, Y., Tian, X., et al. (2021). Sequence stratigraphic characteristics and sedimentary evolution model of the late ediacaran in the Sichuan Basin. *Acta Sedimentol. Sin.* 39 (6), 1440–1450. (in Chinese with English abstract). doi:10.14027/j.issn.1000-0550.2021.119

Peropadre, C., Liesa, C. L., and Meléndez, N. (2013). High-frequency, moderate to high-amplitude sea-level oscillations during the late Early Aptian: Insights into the Mid-Aptian event (Galve sub-basin, Spain). *Sediment. Geol.* 294, 233–250. doi:10.1016/j.sedgeo.2013.05.019

Pittet, B., Van Buchem, F. S., Hillgärtner, H., Razin, P., Grötsch, J., and Droste, H. (2002). Ecological succession, palaeoenvironmental change, and depositional sequences of Barremian–Aptian shallow-water carbonates in northern Oman. *Sedimentology* 49 (3), 555–581. doi:10.1046/j.1365-3091.2002.00460.x

Pomar, L. (2001). Ecological control of sedimentary accommodation: Evolution from a carbonate ramp to rimmed shelf, upper miocene, balearic islands. *Palaeogeogr. Palaeoclimatol. Palaeoecol.* 175 (1-4), 249–272. doi:10.1016/S0031-0182(01)00375-3

Pomar, L., and Haq, B. U. (2016). Decoding depositional sequences in carbonate systems: Concepts vs experience. *Glob. Planet. Change* 146, 190–225. doi:10.1016/j.gloplacha.2016.10.001

Preto, N., Klügel, A., Himmler, T., and Franceschi, M. (2019). Origin of facies zonation in microbial carbonate platform slopes: Clues from trace element and stable isotope geochemistry (Middle Triassic, Dolomites, Italy). *Sedimentology* 66 (1), 81–101. doi:10.1111/sed.12498

Riding, R. (2000). Microbial carbonates: The geological record of calcified bacterial–algal mats and biofilms. *Sedimentology* 47, 179–214. doi:10.1046/j.1365-3091.2000.00003.x

Riding, R. (2011). "Microbialites, stromatolites, and thrombolites," in *Encyclopedia of geobiology*. Editors J. Reitner and V. Thiel (Dordrecht: Springer Netherlands), 635–654. doi:10.1007/978-1-4020-9212-1_196

Rodrigues, M. G., Varejão, F. G., Matos, S. A., Fürsich, F. T., Warren, L. V., Assine, M. L., et al. (2022). High-resolution taphonomy and sequence stratigraphy of internally complex, bakevelliid-dominated coquinas from the Aptian Romualdo Formation, Araripe Basin, NE Brazil. *Mar. Petroleum Geol.* 143, 105814. doi:10.1016/j.marpetgeo.2022.105814

Schröder, S., Grotzinger, J. P., Amthor, J. E., and Matter, A. (2005). Carbonate deposition and hydrocarbon reservoir development at the precambrian–cambrian boundary: The Ara Group in South Oman. *Sediment. Geol.* 180 (1-2), 1–28. doi:10.1016/j.sedgeo.2005.07.002

Shields, G., and Stille, P. (2001). Diagenetic constraints on the use of cerium anomalies as palaeoseawater redox proxies: An isotopic and REE study of cambrian phosphorites. *Chem. Geol.* 175 (1–2), 29–48. doi:10.1016/S0009-2541(00)00362-4

Shields-Zhou, G., Zhu, M., Li, D., Wang, D., and Zhu, M. (2013). Cerium anomaly variations in Ediacaran–earliest Cambrian carbonates from the Yangtze Gorges area, South China: Implications for oxygenation of coeval shallow seawater. *Precambrian Res.* 225, 110–127. doi:10.1016/j.precamres.2011.10.011

Stüeken, E. E., Jones, S., Raub, T. D., Prave, A. R., Rose, C. V., Linnekogel, S., et al. (2020). Geochemical fingerprints of seawater in the late mesoproterozoic midcontinent rift, north America: Life at the marine-land divide. *Chem. Geol.* 553, 119812. doi:10.1016/j.chemgeo.2020.119812

Suarez-Gonzalez, P., Arenas, C., Benito, M. I., and Pomar, L. (2019). Interplay between biotic and environmental conditions in pre-salt messinian microbialites of the Western mediterranean (upper miocene, mallorca, Spain). *Palaeogeogr. Palaeoclimatol. Palaeoecol.* 533, 109242. doi:10.1016/j.palaeo.2019.109242

Sun, Y., Zhang, Y., Xi, A., Tang, Y., Zhou, R., Liu, D., et al. (2022). Petrographic and geochemical characteristics of oncolites in the ediacaran Dengying Formation of the upper

Yangtze area, China: Implications for their paleo-environment. *Sediment. Geol.* 442, 106296. doi:10.1016/j.sedgeo.2022.106296

Taylor, S. R., and McClennan, S. M. (1985). *The continental crust: Its composition and evolution* (Oxford: Blackwell), 312. doi:10.1086/629067

Tang, Q., Cui, H., and Zhang, F. (2022). Neoproterozoic earth-life system. *Precambrian Res.* 368, 106486. doi:10.1016/j.precamres.2021.106486

Tostevin, R., Shields, G. A., Tarbuck, G. M., He, T., Clarkson, M. O., and Wood, R. A. (2016). Effective use of cerium anomalies as a redox proxy in carbonate-dominated marine settings. *Chem. Geol.* 438, 146–162. doi:10.1016/j.chemgeo.2016.06.027

Vahrenkamp, V. C., and Swart, P. K. (1994). "Late cenozoic dolomites of the Bahamas: Metastable analogues for the Genesis of ancient platform dolomites," in *Dolomites: A volume in honour of Dolomieu*. Editors B. Purser, M. Tucker, and D. Zenger (Hoboken, NJ: John Wiley & Sons, Ltd.), Vol. 21, 133–153. doi:10.1002/9781444304077.ch9

Wang, J., He, Z., Zhu, D., Liu, Q., Ding, Q., Li, S., et al. (2020). Petrological and geochemical characteristics of the botryoidal dolomite of Dengying Formation in the Yangtze craton, South China: Constraints on terminal ediacaran "dolomite seas". *Sed. Geol.* 406, 105722. doi:10.1016/j.sedgeo.2020.105722

Wang, L., Hu, G., Zhao, D., Tan, X., and Wang, H. (2022). Microbialites of terminal ediacaran in the upper Yangtze platform, China: From mesoscopic to nanoscale. *Palaeogeogr. Palaeoclimatol. Palaeoecol.* 585, 110729. doi:10.1016/j.palaeo.2021.110729

Wang, Y., Wang, S., Yan, H., Zhang, Y., Li, J., and Ma, D. (2021). Microbial carbonate sequence architecture and depositional environments of member IV of the late ediacaran Dengying Formation, gaoshiti–moxi area, Sichuan Basin, southwest China. *Geol. J.* 56 (8), 3992–4015. doi:10.1002/gj.4146

Webb, G., and Kamber, B. (2000). Rare Earth elements in Holocene reefal microbialites: A new shallow seawater proxy. *Geochimica Cosmochimica Acta* 64 (9), 1557–1565. doi:10.1016/s0016-7037(99)00400-7

Wei, G., Du, J., Xu, C., Zou, C., Yang, W., Shen, P., et al. (2015). Characteristics and accumulation modes of large gas reservoirs in Sinian-Cambrian of Gaoshiti-Moxi region, Sichuan Basin. *Acta Pet. Sin.* 36, 1–12. (in Chinese with English abstract). doi:10.7623/syxb201501001

Wei, M., Bao, Z., Munnecke, A., Liu, W., Harrison, G. W. M., Zhang, H., et al. (2021). Paleoenvironment of the lower–middle cambrian evaporite series in the tarim basin and its impact on the organic matter enrichment of shallow water source rocks. *Minerals* 11 (7), 659. doi:10.3390/min11070659

Wei, W., and Algeo, T. J. (2020). Elemental proxies for paleosalinity analysis of ancient shales and mudrocks. *Geochimica Cosmochimica Acta* 287, 341–366. doi:10.1016/j.gca.2019.06.034

Wen, L., Wang, W. Z., Li, L. J., Hong, H. T., Luo, B., Zhang, X. H., et al. (2020). New understandings of distribution characteristics of Sinian Dengying Formation in southwestern Sichuan Basin and its significance of oil and gas geological exploration. *China Pet. Explor.* 25, 56–65. (in Chinese with English abstract). doi:10.3969/j.issn.1672-7703.2020.03.006

Xu, Z. H., Lan, C. J., Hao, F., Chen, H. R., Yang, W. Q., Ma, X. L., et al. (2020). Difference of mound-bank complex reservoir under different palaeogeographic environment of the Sinan Dengying Formation in Sichuan Basin. *J. Palaeogeogr.* 22, 235–250. (In Chinese with English abstract.). doi:10.7605/gdlxb.2020.02.074

Yan, H., He, D., Jia, A., Li, Z., Guo, J., Peng, X., et al. (2022). Characteristics and development model of karst reservoirs in the fourth member of Sinian Dengying Formation in central Sichuan Basin, SW China. *Petroleum Explor. Dev.* 49 (4), 810–823. doi:10.1016/S1876-3804(22)60312-4

Yang, X., Li, Z., Gao, B., and Zhou, Y. (2021). The Cambrian Drumian carbon isotope excursion (DICE) in the Keping area of the northwestern Tarim Basin, NW China. *Palaeogeogr. Palaeoclimatol. Palaeoecol.* 571, 110385. doi:10.1016/j.palaeo.2021.110385

Zhang, B. M., Liu, J. J., Bian, L. Z., Shen, Y. M., Jia, J. H., Zhang, L. P., et al. (2009). Reef-banks and reservoir-constructive diagenesis. *Earth Sci. Front.* 16, 270–289.

Zhang, B., and Zheng, D. (2022). Sedimentological, geochemical, and geochronological constraints on the origin of the neoproterozoic luoquan formation at the southern margin of the north China craton. *Int. Geol. Rev.* 64 (7), 911–932. doi:10.1080/00206814.2021.1894609

Zhang, F., Xiao, S., Kendall, B., Romaniello, S. J., Cui, H., Meyer, M., et al. (2018). Extensive marine anoxia during the terminal Ediacaran Period. *Sci. Adv.* 4 (6), eaan8983. doi:10.1126/sciadv.aan8983

Zhang, J., Zhang, B. M., and Shan, X. Q. (2014). Controlling effects of paleo-climate and paleo-ocean on formation of carbonate reservoirs. *Petroleum Explor. Dev.* 41, 135–143. doi:10.1016/S1876-3804(14)60016-1

Zhang, X., Shu, D., Han, J., Zhang, Z., Liu, J., and Fu, D. (2014). Triggers for the cambrian explosion: Hypotheses and problems. *Gondwana Res.* 25 (3), 896–909. doi:10.1016/j.gr.2013.06.001

Zhao, G., and Cawood, P. A. (2012). Precambrian geology of China. *Precambrian Res.* 222-223, 13–54. doi:10.1016/j.precamres.2012.09.017

Zheng, J., Zhu, Y., Huang, L., Yang, G., and Hu, F. (2022). Geochemical characteristics and their geological significance of lower cambrian xiaoerblak Formation in northwestern tarim basin, China. *Minerals* 12 (6), 781. doi:10.3390/min12060781

Zhou, Y., Yang, F., Ji, Y., Zhou, X., and Zhang, C. (2020). Characteristics and controlling factors of dolomite karst reservoirs of the Sinian Dengying Formation, central Sichuan Basin, southwestern China. *Precambrian Res.* 343, 105708. doi:10.1016/j.precamres.2020.105708

Zhu, D., Liu, Q., Wang, J., Ding, Q., and He, Z. (2021). Stable carbon and oxygen isotope data of Late Ediacaran stromatolites from a hypersaline environment in the Tarim Basin (NW China) and their reservoir potential. *Facies* 67 (3), 25. doi:10.1007/s10347-021-00633-0

Zhu, D., Liu, Q., Wang, J., Hu, G., and Ding, Q. (2022). Transition of seawater conditions favorable for development of microbial hydrocarbon source–Reservoir assemblage system in the Precambrian. *Precambrian Res.* 374, 106649. doi:10.1016/j.precamres.2022.106649

Zhu, G., Wang, T., Xie, Z., Xie, B., and Liu, K. (2015). Giant gas discovery in the Precambrian deeply buried reservoirs in the Sichuan Basin, China: Implications for gas exploration in old cratonic basins. *Precambrian Res.* 262, 45–66. doi:10.1016/j.precamres.2015.02.023

Zhu, M., Zhang, J., and Yang, A. (2007). Integrated ediacaran (sinian) chronostratigraphy of South China. *Palaeogeogr. Palaeoclimatol. Palaeoecol.* 254, 7–61. doi:10.1016/j.palaeo.2007.03.025

Zou, C., Du, J., Xu, C., Wang, Z., Zhang, B., Wei, G., et al. (2014). Formation, distribution, resource potential, and discovery of Sinian–Cambrian giant gas field, Sichuan Basin, SW China. *Petroleum Explor. Dev.* 41 (3), 306–325. doi:10.1016/s1876-3804(14)60036-7